

Modified Aerotaxy for the Plug-in Manufacture of Cell-Penetrating Fenton Nanoagents for Reinforcing Chemodynamic Cancer Therapy

Kishwor Poudel,[#] Kang Sik Nam,[#] Jiseok Lim,[#] Sae Kwang Ku, Jungho Hwang,^{*} Jong Oh Kim,^{*} and Jeong Hoon Byeon^{*}



Cite This: *ACS Nano* 2022, 16, 19423–19438



Read Online

ACCESS |

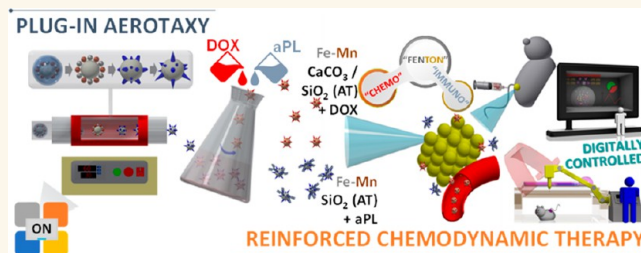
Metrics & More

Article Recommendations

Supporting Information

ABSTRACT: The assemblies of anisotropic nanomaterials have attracted considerable interest in advanced tumor therapeutics because of the extended surfaces for loading of active molecules and the extraordinary responses to external stimuli for combinatorial therapies. These nanomaterials were usually constructed through templated or seed-mediated hydrothermal reactions, but the lack of uniformity in size and morphology, as well as the process complexities from multiple separation and purification steps, impede their practical use in cancer nanotherapy. Gas-phase epitaxy, also called aerotaxy (AT), has been introduced as an innovative method for the continuous assembly of anisotropic nanomaterials with a uniform distribution. This process does not require expensive crystal substrates and high vacuum conditions. Nevertheless, AT has been used limitedly to build high-aspect-ratio semiconductor nanomaterials. With these considerations, a modified AT was designed for the continuous in-flight assembly of the cell-penetrating Fenton nanoagents (Mn–Fe CaCO_3 (AT) and Mn–Fe SiO_2 (AT)) in a single-pass gas flow because cellular internalization activity is essential for cancer nanotherapeutics. The modified AT of Mn–Fe CaCO_3 and Mn–Fe SiO_2 to generate surface nanoroughness significantly enhanced the cellular internalization capability because of the preferential contact mode with the cancer cell membrane for Fenton reaction-induced apoptosis. In addition, it was even workable for doxorubicin (DOX)-resistant cancer cells after DOX loading on the nanoagents. After combining with immune-checkpoint blockers (antiprogrammed death-ligand 1 antibodies), the antitumor effect was improved further with no systemic toxicity as chemo-immuno-chemodynamic combination therapeutics despite the absence of targeting ligands and external stimuli.

KEYWORDS: anisotropic nanomaterials, modified aerotaxy, Fenton nanoagents, cellular internalization, chemo-immuno-chemodynamic combination therapeutics



Developing a modular, convenient, robust, and low-cost assembly system to build biofunctional nanomaterials is a significant challenge in cancer therapy. Such a nanomaterial must ensure improved tumor suppression, blood circulation, targetability, bioavailability, and stimulus-response behavior, including reduced systemic toxicity.^{1–3} Recently, anisotropic (nonspherical) nanomaterials have attracted considerable attention for cancer therapy because modulating the material geometry is crucial in cellular internalization and interactions with cell membranes and biodistribution and cytotoxicity.^{4–8} In particular, the characteristic curvatures of the anisotropy generate preferential contact with the cell membranes that can enhance internalization^{9–11} and offer

prolonged *in vivo* circulation owing to the characteristic oscillation and lateral drift.^{12,13} On the other hand, complex and harsh assembly procedures with low yield and productivity on the nanoscale impede the clinical translation of anisotropic nanomaterials.^{14–17} Hence, digitizable continuous flow approaches operating under a steady state are highly recom-

Received: September 13, 2022

Accepted: October 14, 2022

Published: October 18, 2022



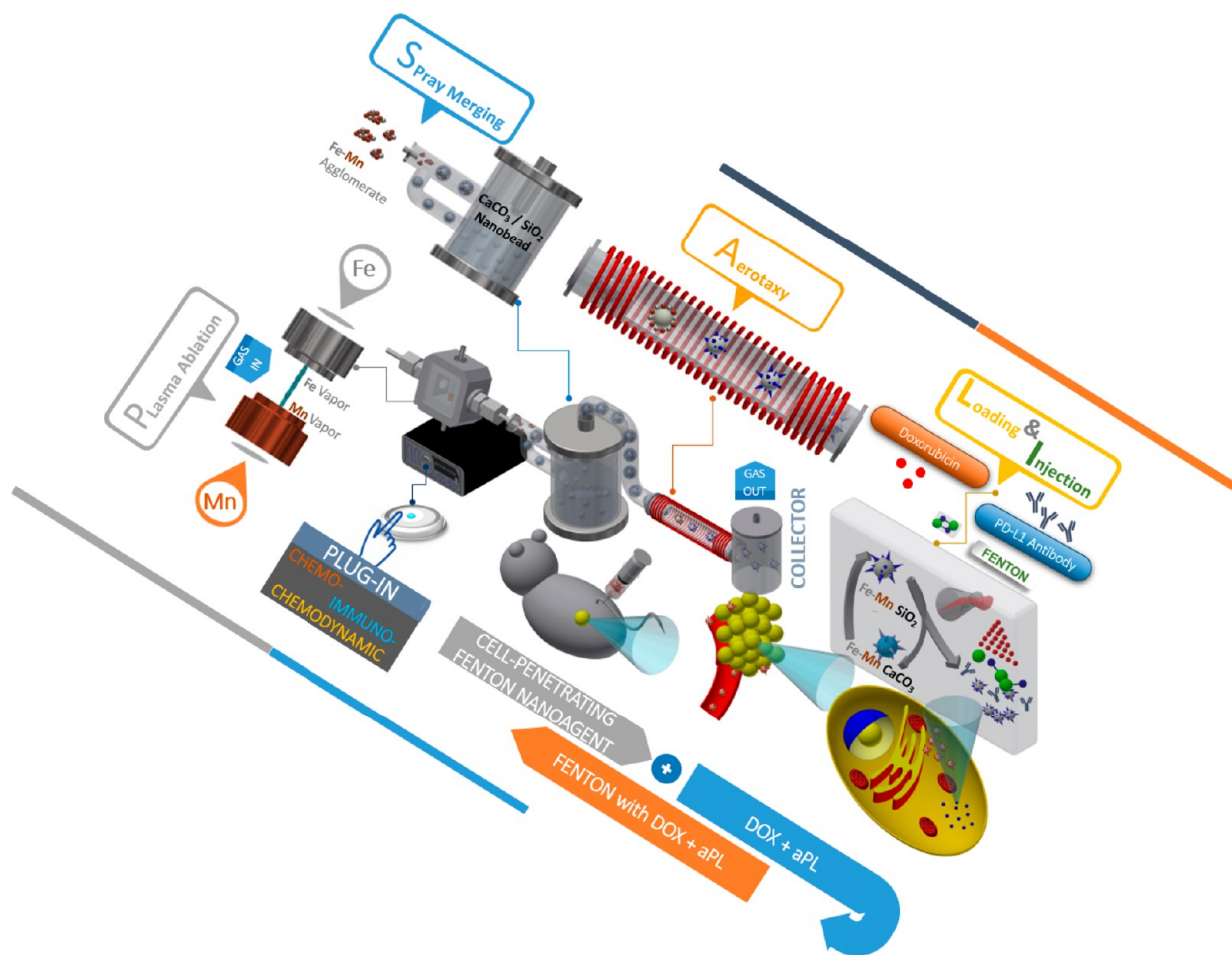


Figure 1. Illustration of the modified AT for the plug-in assembly of the anisotropic Fenton nanoagents. Coinjection of the Mn–Fe agglomerates from a spark plasma and amorphous CaCO_3 or SiO_2 nanobeads from a mechanical spray into an orifice was carried out in a nitrogen gas flow to prepare the composite precursors (Mn–Fe CaCO_3 and Mn–Fe SiO_2). The precursors were then passed through a heated tube reactor to achieve the AT of Mn–Fe on the nanobeads in the presence of sheath air flow to form MnFe_2O_4 nanospikes as the anisotropic Fenton nanoagents. The resulting nanoagents were combined with DOX and aPL to reinforce the chemodynamic therapy without external stimuli and targeting ligands.

mended to provide reproducible and controllable assemblies on a large scale in connection with the computed platforms (e.g., artificial intelligence, neural networks, and machine learning) for anticancer nanomedicines.^{18–20}

The NanoLund group introduced gas-phase epitaxy, also called aerotaxy (AT), as an approach to continuously produce anisotropic nanomaterials with high growth rates in a controllable manner without the need for expensive single-crystal substrates and high vacuum conditions.^{21–23} The formation and manipulation of anisotropic nanomaterials were achieved in a continuous stream of gas with evaporation–condensation (seed particle formation) and gaseous inorganic precursor injection into a high-temperature flow reactor (epitaxial growth on the seed particle). This method has been used mainly to manufacture anisotropic semiconductor nanomaterials, and the utilization of the manufactured material has been limited to optoelectronic devices despite its broad-spectrum potential.^{24,25}

Motivated by the above discussions, this study designed and constructed a modified AT system through a serial connection of electrically operable aerosol dispensers and a heated flow reactor to manufacture Mn–Fe spike decorated amorphous CaCO_3 (denoted as Mn–Fe CaCO_3 (AT)) and SiO_2 (denoted

as Mn–Fe CaCO_3 (AT)) nanoagents for chemodynamic cancer therapies in a single-pass, continuous configuration, unlike multistep wet chemical processes (Table S1). The modified AT used a spark plasma to ablate the transition metals (Mn and Fe) and a mechanical spray to supply amorphous biocompatible CaCO_3 ²⁶ and SiO_2 ²⁷ nanobeads as a digital manufacture platform^{28–30} to generate Mn–Fe CaCO_3 and Mn–Fe SiO_2 composite precursors for the in-flight epitaxial growth of anisotropic Mn–Fe oxides (MnFe_2O_4) on nanobeads. The resulting Mn–Fe CaCO_3 (AT) and Mn–Fe SiO_2 (AT) were assessed as biofunctional nanoagents for Fenton reaction-induced cancer treatment (i.e., chemodynamic therapy from hydroxyl radicals that lead to high oxidative stress in tumor cells). This is because the therapy is a practical approach to ensure high therapeutic specificity, tumor selectivity, and low invasiveness to mitigate systemic side effects without external stimulation.^{31–34} Integrating Mn and Fe metals was selected for the AT because both Mn and Fe ions are effective in producing hydroxyl radicals in the presence of hydrogen peroxide in the tumor microenvironment through the Fenton reactions ($\text{Mn}^{2+} + \text{H}_2\text{O}_2 \rightarrow \text{Mn}^{3+} + \cdot\text{OH} + \text{OH}^-$ and $\text{Fe}^{2+} + \text{H}_2\text{O}_2 \rightarrow \text{Fe}^{3+} + \cdot\text{OH} + \text{OH}^-$)^{35–38} while benefiting in the physicochemical property associated with each

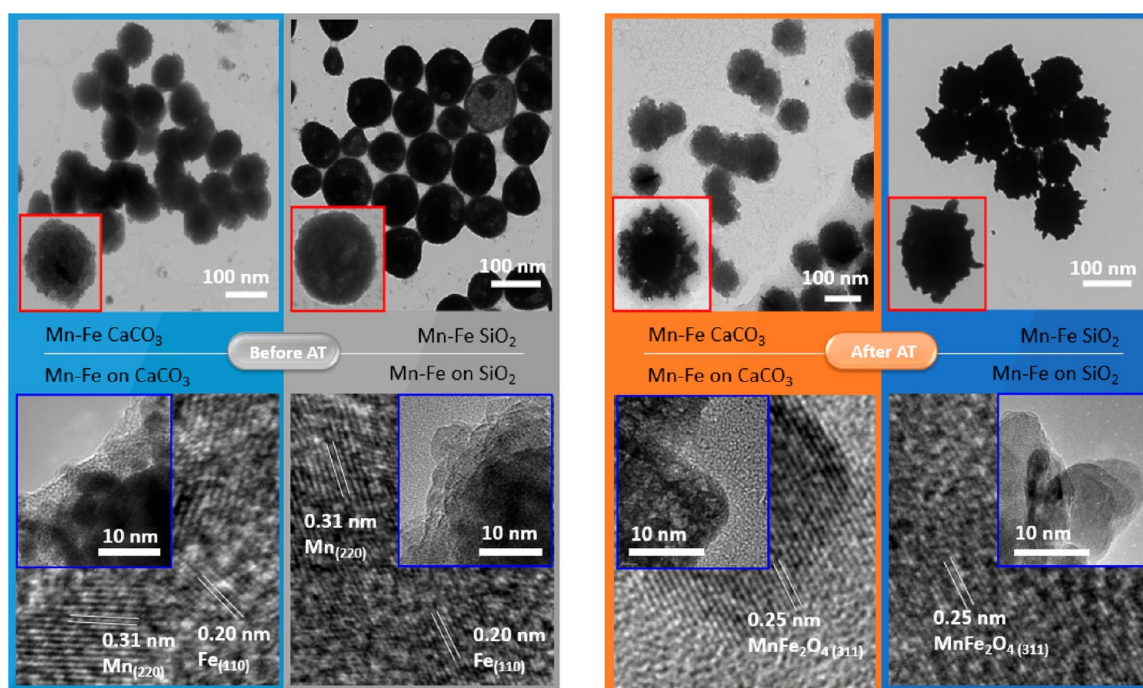


Figure 2. Morphological analyses of the nanoagents (after AT), including the composite precursors (before AT) for comparison. Low- and high-magnification TEM images of the nanoagents with Mn–Fe and epitaxially grown MnFe_2O_4 on the nanobeads are displayed in different columns. The lattice spacings at the outer region of the composite precursors matched the individual Mn and Fe crystals, while MnFe_2O_4 protruded at the region after passing through the heated tube reactor. Changing the core nanobeads from CaCO_3 to SiO_2 induced a difference in the shape of the MnFe_2O_4 protrusions.

component from the bimetallic configuration.³⁹ In previous reports, CaCO_3 and SiO_2 nanoparticles were used as the base materials for Fenton reaction-based cancer treatments to boost the therapeutic efficacy with no adverse effects,^{40,41} leading this study to utilize Mn–Fe CaCO_3 and Mn–Fe SiO_2 as precursors for AT.

In modified AT (Figure 1), spark plasma produced the Mn–Fe agglomerates. The mechanical spray generated CaCO_3 or SiO_2 nanobeads were passed through an orifice to construct Mn–Fe CaCO_3 or Mn–Fe SiO_2 composite precursors in the aerosol state. The precursor particles were then passed through a heated tube reactor for the epitaxial growth of anisotropic MnFe_2O_4 on nanobeads in the presence of sheath air under single-pass flow. The resulting particles (Mn–Fe CaCO_3 (AT) and Mn–Fe SiO_2 (AT) nanoagents), including the composite precursors (Mn–Fe CaCO_3 and Mn–Fe SiO_2 before AT) for comparison, were collected on hydrophobic substrates and their physicochemical properties were characterized. The particles were dispersed in buffered saline to assess the internalization, reactive oxygen species (ROS) production, apoptosis, and cytotoxic activity to EMT6 (a murine mammary carcinoma) cells under a range of conditions (normoxic and hypoxic). Doxorubicin (DOX) and anti-programmed death-ligand 1 antibody (aPL; immune-checkpoint blocker (ICB)) were loaded for combinatorial chemodynamic therapy with biodistribution and biosafety assays based on DOX resistance (EMT6R) (Figures 1 and S1). Targeting ligands and external stimuli were not used to demonstrate a convenient and straightforward strategy for reinforcing chemodynamic cancer therapy using only clinically approved DOX (increasing hydrogen peroxide concentration in tumor cells)⁴² and aPL (blocking immunosuppressive pathways)⁴³ with nanoagents from modified AT.

RESULTS AND DISCUSSION

The optimal AT conditions for biosafety were determined by first measuring the hemolytic activity of the nanoagent and composite precursor particles as the degree of red blood cell destruction (percentage hemolysis) after incubation with the particles. Hemolysis was obtained after exposure to the particles at a high concentration (500 $\mu\text{g}/\text{mL}$) in phosphate-buffered saline (PBS). Figure S2 presents the results under the AT conditions (3 kV, 1 kHz for spark plasma; 0.3 MPa, 2 l/min for mechanical spray, 1050 $^\circ\text{C}$, 1 l/min sheath air for in-flight epitaxy). No significant hemolytic effects (<4%) were observed, but there were slight differences between the particle samples, representing neglectable increases in hemotoxicity for the applications of AT. The limited levels of hemolysis of the resulting particles indicated the hemocompatibility for systemic circulation, warranting further investigation for *in vitro* and *in vivo* anticancer tests, including the physicochemical characterization of the particles.

The changes in the in-flight size distribution between the nanoagents (after AT; Mn–Fe CaCO_3 (AT) and Mn–Fe SiO_2 (AT)) and composite precursors (before AT; Mn–Fe CaCO_3 and Mn–Fe SiO_2) were identified using a scanning mobility particle sizer (SMPS) by directly sampling the particle-laden gas flow. The average geometric mean diameter (GMD) of the two precursors were 93.8 and 92.1 nm, respectively, which were increased by 108.6 and 108.9 nm after AT (Figure S3A) despite no additional peaks in the size distribution. The geometric standard deviations (GSD) of the two nanoagents also showed higher values than those of the precursors, suggesting that the sizes of the individual precursor particles were enlarged without structural cleavage after AT. This may be due to the restructuring of Mn–Fe particles on CaCO_3 or SiO_2 nanobeads caused by epitaxial growth in the heated tube

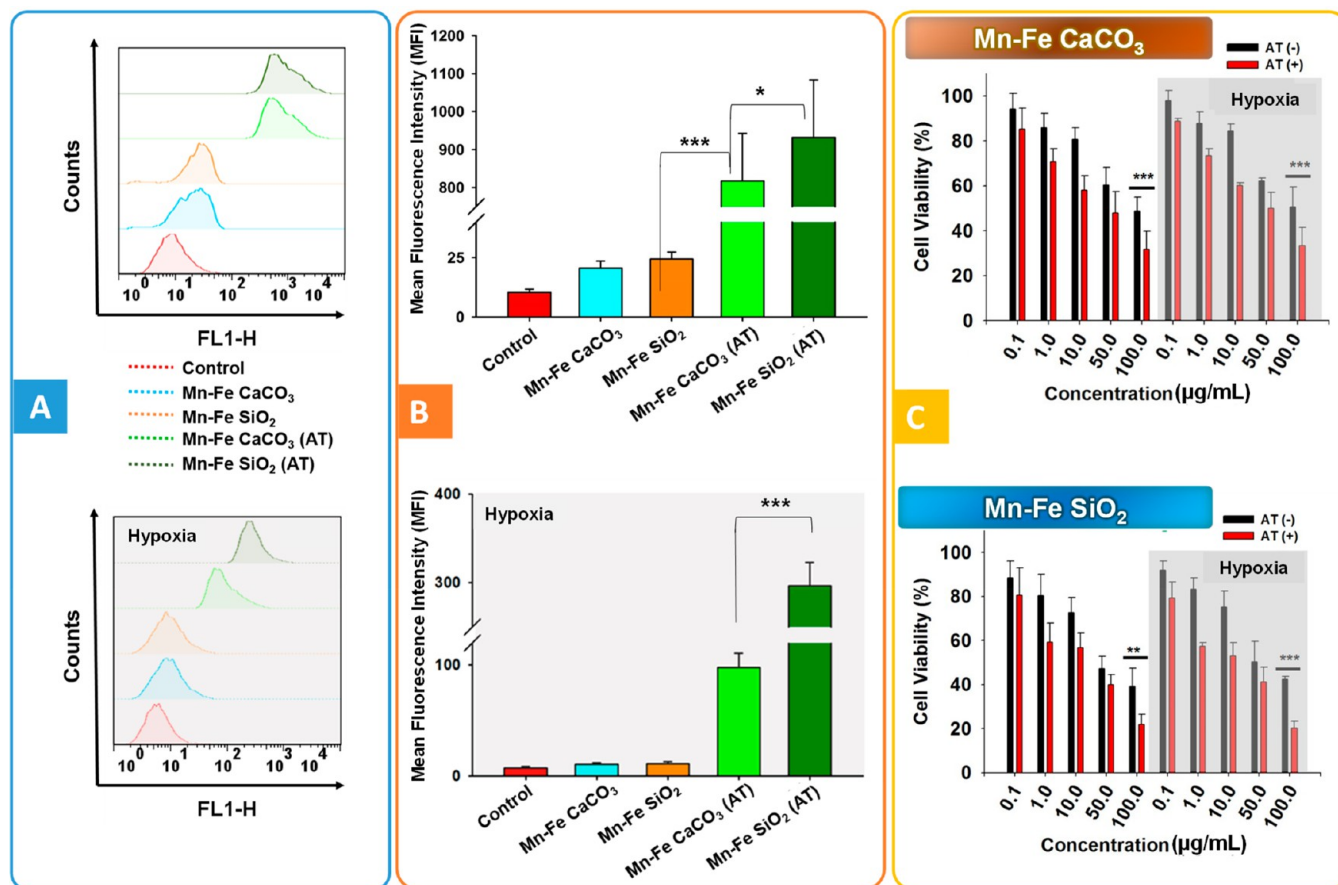


Figure 3. Internalization and cytotoxic activity of the nanoagents (Mn-Fe CaCO₃ (AT) and Mn-Fe SiO₂ (AT)) and composite precursors (Mn-Fe CaCO₃ and Mn-Fe SiO₂) for EMT6 cells under normoxic and hypoxic conditions. (A, B) FACS profiles and their quantified plots (MFI) representing the internalization of coumarin-6 loaded (1 µg/mL) nanoagents into EMT6 cells after 1 h incubation. (C) Viability profiles of EMT6 cells treated with the nanoagents (AT (+)) and composite precursors (AT (-)) for 24 h under normoxic and hypoxic conditions. **p* < 0.05, ***p* < 0.01, ****p* < 0.001.

reactor, increasing the GMD and GSD. This phenomenon was supported by the similarity between the nanoagents and precursors in the total number concentration (TNC). As shown in Figure S3B, the increase in size after AT was also observed by dynamic light scattering (DLS) after dispersing the nanoagent and precursor particles in PBS (pH 7.4). The particle sizes imperfectly matched the sizes from the SMPS measurements because of their different measurement principles and dispersion media.⁴⁴ The polydispersity indices from the DLS measurements were lower than 0.3, indicating acceptable values for a homogeneous population of nano-carriers.^{45,46} The zeta potentials of the resulting particles were also obtained using DLS, in which the particles exhibited negative surface charges at the physiological pH, and there were no significant differences between the nanoagents (−37 mV) and precursors (−36 mV). This suggests that the AT in the gas flow did not alter the electrostatic surface polarity of the resulting particles because there were no positrons in the experimental gas and air environment.⁴⁷

The morphological differences between the nanoagent and composite precursor particles were observed by transmission electron microscopy (TEM) of particles collected on carbon-coated copper grids (Figure 2). The left panel showed low- and high-magnification images of the precursor particles, where fine dark dots were densely distributed on the spherical domains (i.e., CaCO₃ and SiO₂ nanobeads). High-magnification images

of the outermost aggregated dots of the particles exhibited the characteristic lattice spacings of individual Mn ($d_{\text{Mn}, 220} = 0.31$ nm) and Fe ($d_{\text{Fe}, 110} = 0.20$ nm).^{48,49} No alloyed Mn-Fe was detected. This may be due to the rapid quenching of the two metal vapors from the spark plasma in the presence of room temperature nitrogen gas flow to form aggregates consisting of individual Mn and Fe particles (Figure S4) and to the significant difference in the lattice spacings of Mn and Fe. This shows that the cocurrent flow of monometallic Mn and Fe particles and CaCO₃ (or SiO₂) nanobeads for passing through an orifice in the mechanical spray in the serial connection enabled the in-flight incorporation of the particles and nanobeads before entering the heated tube reactor for the AT. The right panel showed spiky surfaces on the nanobeads, and the lattice spacing matched the characteristic microstructure of MnFe₂O₄ ($d_{\text{MnFe}_2\text{O}_4, 311} = 0.25$ nm).^{50,51} The compositional change may be due to the oxidation of Mn-Fe aggregates in the presence of sheath air, while the surface anisotropy is related to the transformation strain ($\epsilon = (-\Delta S/V_m)(d\sigma_0/dT)^{-1}$, where ΔS , V_m , and $d\sigma_0/dT$ are the entropy change from the parent phase, molar volume, and critical stress temperature dependence, respectively)⁵² depending on the crystallographic orientation during AT that enables the anisotropic epitaxial growth of Mn-Fe with the inclusion of oxygen to form MnFe₂O₄ nanospikes. The differences in spike shape between Mn-Fe CaCO₃ (AT) and Mn-Fe SiO₂ (AT)

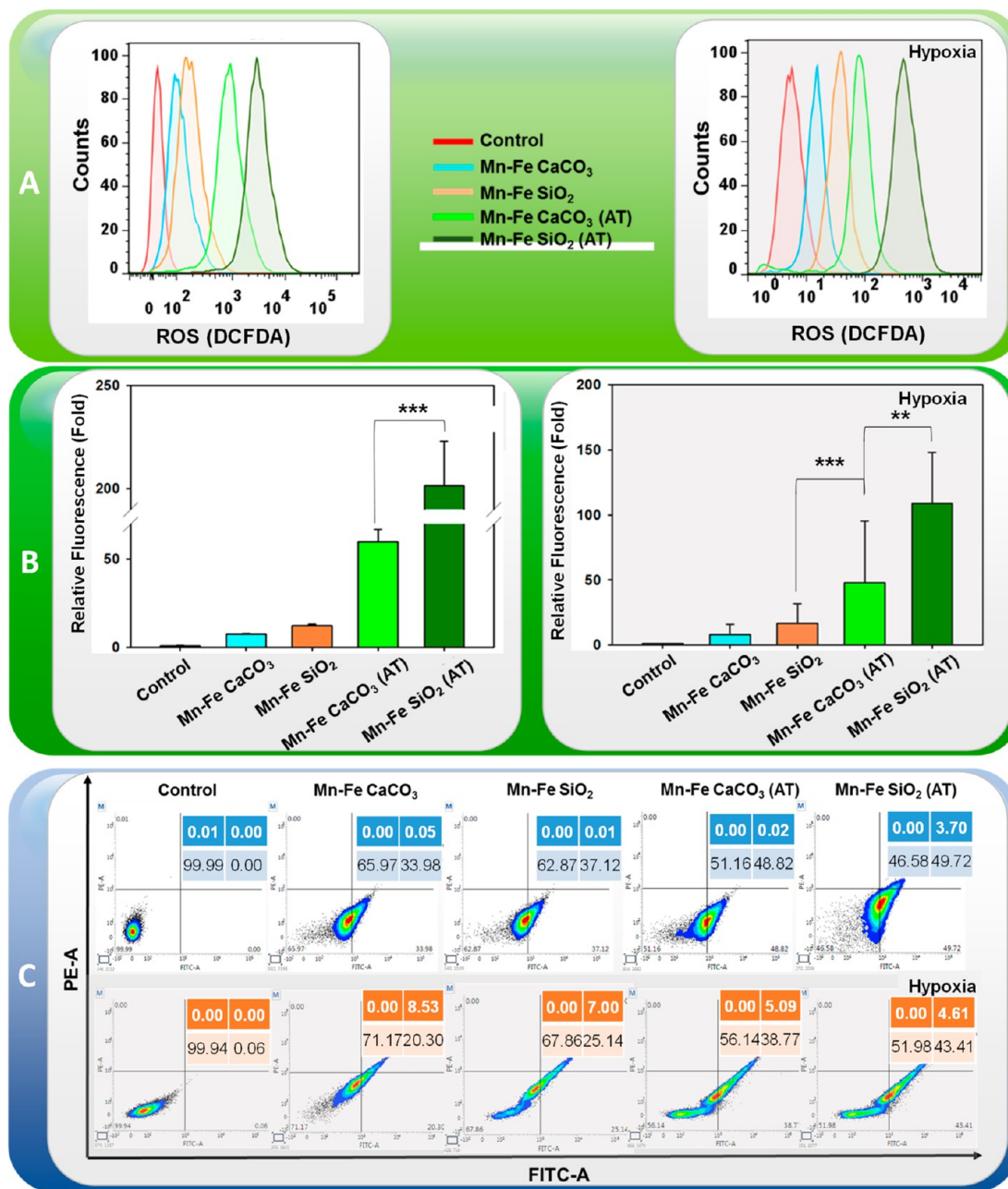


Figure 4. ROS generation and apoptotic activity of the nanoagents and composite precursors for EMT6 cells under normoxic (white boxes) and hypoxic (gray boxes) conditions. (A, B) FACS profiles and their quantified fluorescent plots to examine the cellular ROS generation. (C) Apoptosis in the cells incubated with the nanoagents and composite precursors for 24 h. * $p < 0.05$, ** $p < 0.01$, *** $p < 0.001$.

may be due to the textural properties (Figure S5) of the amorphous CaCO₃ and SiO₂ nanobeads (Figure S4).^{53,54} The differences in the resulting contrast of the nanobeads representing a microstructural difference were examined by TEM, which were attributed to differences in specific surface area, average pore diameter, and adsorption–desorption isotherm, resulting in the formation of different surface textures to generate different orientations of Mn–Fe aggregates during AT.⁵⁵ These textural-induced differences in the pattern of epitaxial growth were attributed to the different capillarity ($E_{\text{cap}} = -2rl \cos \theta_E$, where E_{cap} , r , l , and θ_E are the energy gain for the capillary filling of a bead, radius of the inner cavity, length of the cavity, and equilibrium contact angle, respectively)⁵⁶ inside the cavities of nanobeads affecting the

anisotropic growth of MnFe₂O₄ during AT. This suggests that the modified AT is a workable process for ensuring reconfigurable surface anisotropy on the nanobeads in a single-pass configuration without using expensive crystal substrates and high vacuum conditions. X-ray diffraction (XRD) showed the coexistence of the characteristic bands for MnFe₂O₄^{57,58} and amorphous CaCO₃ (or SiO₂) (Figure S6A),^{59,60} presenting the growth of MnFe₂O₄ on the nanobeads during AT. The oxidized surface states of Mn (2p) and Fe (2p) compared to those of the zerovalent counterparts for Mn–Fe SiO₂ (AT) with O (1s) spectrum in the core level X-ray photoelectron spectra (XPS) further supported the growth of MnFe₂O₄ (Figure S6B–D).^{61,62} The oxidized states (also represented as positive charge current

values of the nanoagents in the aerosol state, as shown in Figure S3B) may adsorb the negative charges in PBS, which was also relevant to the negative polarities of the nanoagents in the zeta potential measurements. In addition, susceptibility to surface modification was primarily tested by incorporating polyethylenimine (PEI) transfection agent on the resulting nanoagents. Plasmid DNA (pDNA) was loaded on the nanoagents in the absence and presence of PEI to form nanoagent-gene complexes for exposure to EMT6 cells. As shown in Figure S6E, the PEI incorporation with nanoagents significantly enhanced the transfection efficiency probably due to positively charged surface groups of the PEI (exhibiting positive zeta potential) on the nanoagents, which was even higher than that of lipofectamine-gene complexes as a comparative case, suggesting surface modifiable property of the nanoagents with targeting moieties.

Based on the rougher surfaces after AT, internalizing nanoagent and composite precursor particles were examined and compared using normoxic and hypoxic EMT6 cells because hypoxia usually deteriorates the therapeutic efficacy of the Fenton reaction-inducing nanoparticles.⁶³ The comparison in internalization behavior between the nanoagent and composite precursor particles was first conducted through fluorescence-activated cell sorting (FACS) after a coumarin-6 loading because the cellular uptake of nanoparticles is essential for enhancing the therapeutic efficacy. Higher internalization rates were observed for the nanoagents (after the AT) than those of the composite precursors (before the AT) both under normoxic and hypoxic conditions (Figure 3A,B). From image processing of the TEM images, the nanoagents exhibited a greater average value (1.83) of the aspect ratio (relationship between the width and height of a spike) than that of composite precursors (1.12), which facilitates the higher internalization rates. Under hypoxic conditions, the rates deteriorated simultaneously compared to normoxia regardless of AT. Hence, the internalization is accredited to the energy dependence⁶⁴ rather than the anisotropy of the nanoagents. Nevertheless, the nanoagents (Mn–Fe CaCO₃ (AT) and Mn–Fe SiO₂ (AT)) were highly internalized into the cells compared to the composite precursors, suggesting that spiky exteriors secured by the AT are more effective for internalization because of the better contact.^{65,66} The differences between the Mn–Fe CaCO₃ (AT) and Mn–Fe SiO₂ (AT) nanoagents may be due to the different degrees of anisotropic stiffness that derive the different contacts for internalization. A 3-(4,5-dimethylthiazol-2-yl)-2,5-diphenyltetrazolium bromide (MTT) assay was used to determine the cytotoxic effects of the nanoagent (denoted as AT (+)) and composite precursor (denoted as AT (–)) particles on EMT6 cells at different concentrations (0.1–100.0 μg/mL). As shown in Figure 3C, the cytotoxicity was positively correlated with the internalization rates in normoxia and was even retained under hypoxic conditions. The similar cytotoxic profiles in hypoxia were attributed to the slower growth of hypoxic cells than that of normoxic cells that induce equal or superior killing rates to proliferation.^{67,68} This suggests that additional surface treatments or external stimuli may be effective in modulating the cytotoxic profiles, even in hypoxia. The cytotoxic profiles for the CD8⁺ cocultured cells treated with the nanoagent and composite precursor particles were similar to those of the treated normoxic and hypoxic cells, suggesting that CD8⁺ cells are not significantly impaired by exposure to the particles (Figure S7). ROS production and apoptosis representing the

oxidative damage to the cellular molecules were then determined to elucidate the mechanism of the cytotoxic activity of the nanoagent and composite precursor particles. 2',7'-Dichlorodihydrofluorescein diacetate (DCFDA) was used to examine the oxidative damage to normoxic and hypoxic cells, as shown in Figure 4A (FACS profiles) and B (fluorescent ROS levels). The highest ROS production was observed in the cells treated with the Mn–Fe SiO₂ (AT) nanoagents, which were retained for the hypoxic cells. This may be due to the strongest physical engagement between the spike (from epitaxial growth of MnFe₂O₄ on a SiO₂ nanobead) and the cell membrane, which provides channels for the largest transport of Mn and Fe ions to the cancer cell membrane and the intracellular region for ROS generation by the Fenton-mediated (catalyzed by Fe ions) and Fenton-like (catalyzed by Mn ions) reactions induced the chemodynamic anticancer activity. Atomic absorption spectroscopy detected greater amounts of Mn and Fe ions for the Mn–Fe CaCO₃ (AT; approximately 1.9 times) and Mn–Fe SiO₂ (AT; approximately 3.3 times) compared to Mn–Fe CaCO₃ and Mn–Fe SiO₂ after their dispersion in buffered saline (pH 6.5 at 37 °C) for 48 h. In addition, the different release kinetics of the metal ions from the –Ca/Si–O–Mn/Fe– hybrid frameworks might also affect the difference in ROS production between the Mn–Fe CaCO₃ (AT) and Mn–Fe SiO₂ (AT) nanoagents.⁶⁹ Similar to the internalization and cytotoxicity, ROS generation was reduced under hypoxic conditions because of the relatively lower uptake (led to lower cytotoxicity), showing that the cytotoxicity is related to ROS production. This trend was also retained in the apoptosis of both normoxic and hypoxic cells, as shown in Figure 4C. All particles resulted in early apoptosis of the cells with a minor percentage of late apoptotic cells despite decreases in early apoptosis in the hypoxic cells, strengthening the correlations among the internalization, cytotoxicity, ROS production, and apoptosis.

Considering the enhanced internalization from the AT, the delivery of DOX to EMT6 and EMT6R (DOX-resistant EMT6) cells was attempted and compared after loading the nanoagent and composite precursor particles. EMT6R cells were developed from the consistent incubation of EMT6 cells with DOX in several passages for withstanding the DOX. The half-maximal inhibitory concentration (IC₅₀) for EMT6 and EMT6R cells was estimated using the cytotoxicity assay, and the specific values were 1.52 and 48.41 μg/mL (a more than 30-fold increase in DOX resistance), respectively (Figure S8A). As the major parameters for the DOX efflux, the expression of the P-glycoprotein (P-gp; representing P-gp mediated drug efflux,⁷⁰ as depicted in Figure S8B) and P53 proteins in EMT6 cells (denoted as I) and EMT6R cells (denoted as II) was recorded (Figure S8C) because they are expressed strongly and weakly in the resistant variants, respectively.^{71,72} A substantial upsurge in the expression of P-gp was observed in EMT6R cells compared to EMT6 cells and a prominent decrease in the expression of P53 in EMT6R cells relative to EMT6 cells (Figure S8C), proving DOX resistance. The loading capacity (LC) and entrapment efficiency (EE) of DOX in the nanoagent and composite precursor particles were approximately 9% and 96%, respectively (Figure S9A). No significant differences between the particles were observed, suggesting that AT did not alter these properties despite the morphological changes. Moreover, capillary suction from the porosity range of the core nanobeads (Figure S5) did not show significant differences in the LC and EE of DOX molecules

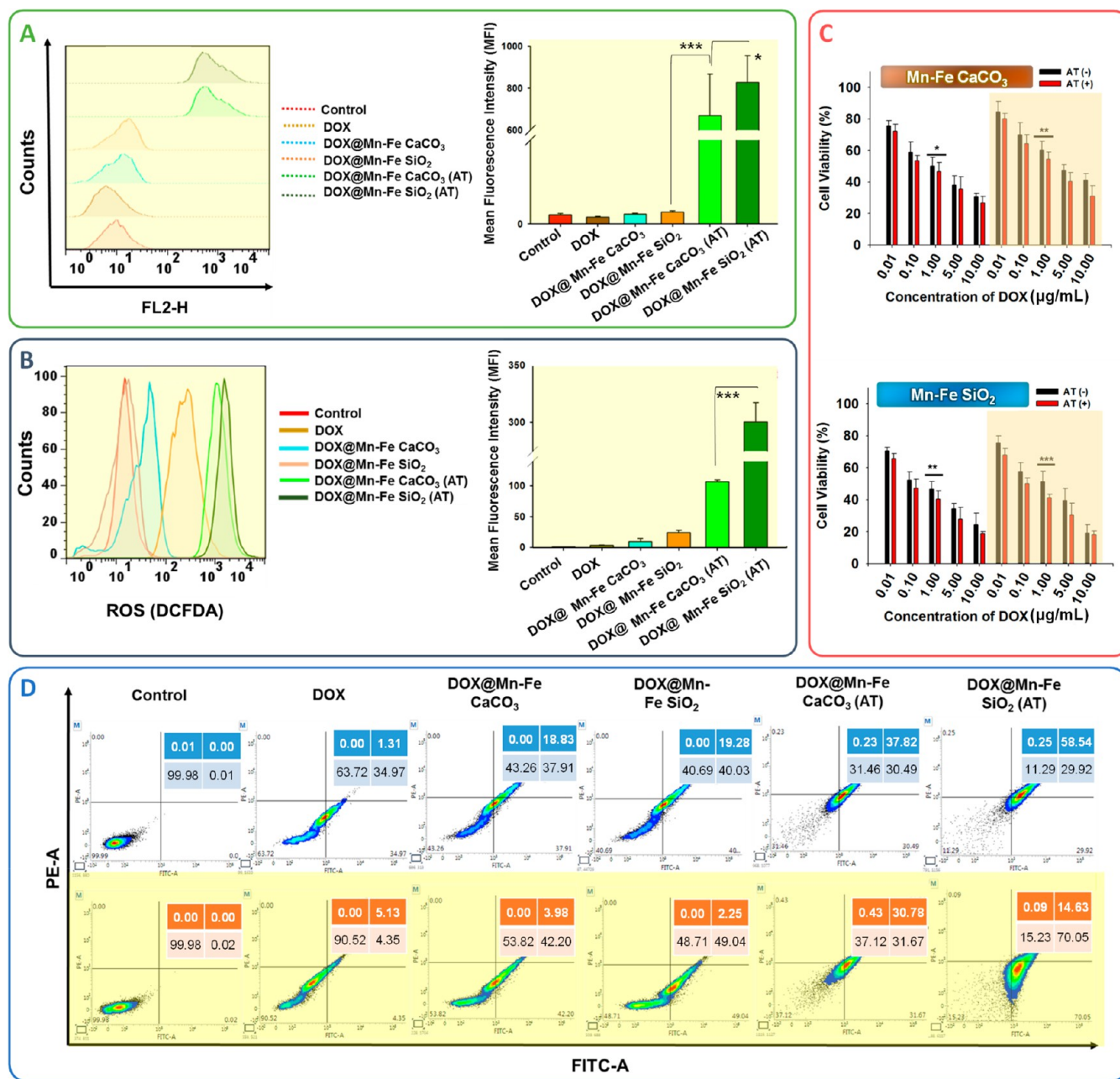


Figure 5. Internalization, ROS generation, and cytotoxic and apoptotic activity of the DOX-loaded nanoagents (DOX@Mn–Fe CaCO₃ (AT) and DOX@Mn–Fe SiO₂ (AT)) and composite precursors (DOX@Mn–Fe CaCO₃ and DOX@Mn–Fe SiO₂) for EMT6R cells (denoted as yellow boxes). (A, B) FACS profiles and their quantified plots (MFI) to examine cellular internalization and ROS generation. (C) Viability profiles of EMT6 (white) and EMT6R (yellow) cells treated with the DOX-loaded (0.01–10.00 µg/mL) nanoagents (AT (+)) and composite precursors (AT (–)) for 24 h. (D) Apoptosis in the EMT6 (white) and EMT6R (yellow) cells treated with DOX loaded nanoagents and composite precursors, including DOX alone for comparison. **p* < 0.05, ***p* < 0.01, ****p* < 0.001.

(1.19–1.53 nm in size).⁷³ In this connection, the nanoagent and composite precursor particles exhibited similar time- and pH-dependent (~69% at pH 7.4 and ~77% at pH 6.5) DOX release profiles for 48 h monitoring (Figure S9B). Regarding the electrostatic interactions between the particles and DOX molecules, the negative surface potential of the particles dispersed in the DOX solution may confer a binding function to the positively charged moieties of DOX to transform into the DOX loaded nanoagent (DOX@Mn–Fe CaCO₃ (AT) and DOX@Mn–Fe SiO₂ (AT)) and composite precursor (DOX@Mn–Fe CaCO₃ and DOX@Mn–Fe SiO₂) particles. In a mildly acidic microenvironment, partial dissociation of the

hydrogen bonding interaction may have occurred due to the protonation of –NH₂ groups of DOX⁷³ that increase the hydrophilicity and release rate. The internalization activity of the DOX-loaded particles into the EMT6R cells was examined and compared with free DOX (Figure 5A). Free DOX was rarely internalized into the resistant cells because of the efflux, while the DOX-loaded Mn–Fe CaCO₃ and Mn–Fe SiO₂ particles exhibited slightly higher internalization. The activity was enhanced significantly for the DOX-loaded nanoagents, suggesting that the surface nanospikes can overcome the efflux. The higher internalization produced similarly higher levels of ROS production as an effective chemo–chemodynamic

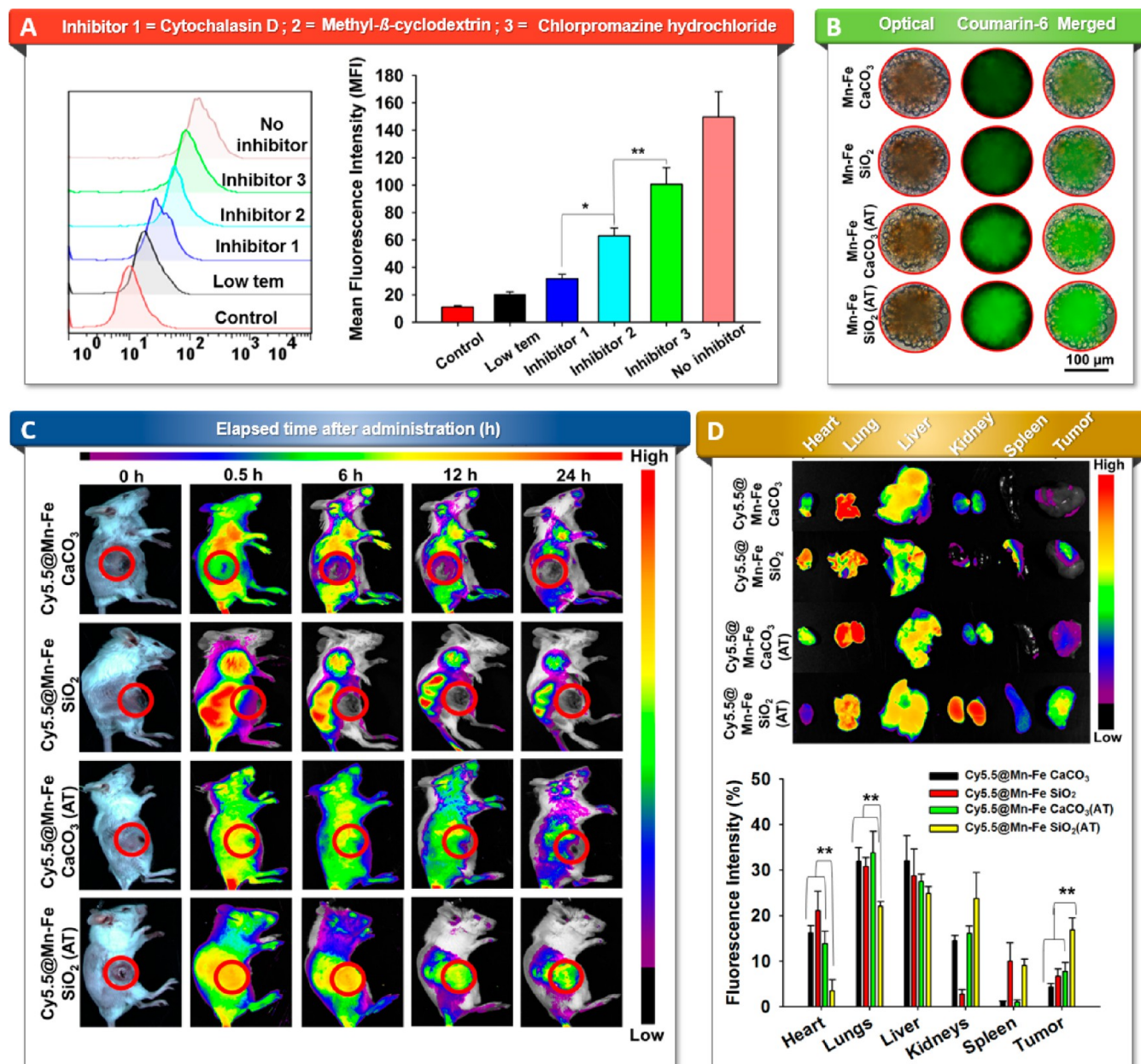


Figure 6. Endocytosis, cell-penetration, and *in vivo* biodistribution characteristics of the nanoagents and composite precursors. (A) FACS profiles and their quantified plots (MFI) to examine the internalization of Mn-Fe SiO₂ (AT) nanoagent into EMT6R cells pretreated with the different inhibitors (1–3), including low-temperature and no inhibitor conditions. (B) Cell-penetrating activity of the coumarin-6 loaded nanoagents and composite precursors into EMT6R spheroids. (C) Fluorescent contours from the *in vivo* biodistribution assay for EMT6R tumor xenografted BALB/C mice after the intravenous administration of the Cy5.5-loaded nanoagents and composite precursors. The fluorescent images were acquired from subcutaneous tumor-bearing BALB/c mice after an intravenous injection of the Cy5.5-loaded (1 μ g/mL) nanoagents and composite precursors. (D) *Ex vivo* fluorescent contours and their quantified plots from excised vital organs and tumors of the tumor-bearing mice sacrificed at 24 h after the intravenous administration. * p < 0.05, ** p < 0.01.

therapeutics than the other configurations (Figure 5B). Owing to this combined activity, the cytotoxic effects of the DOX-loaded particles on EMT6R cells were comparable to those of EMT6 (normal) cells (Figure 5C), even though the differences between AT (+) and AT (–) were not significant compared to the internalization and ROS production profiles due likely to the coexistence of DOX and AT (–) particles (Mn-Fe CaCO₃ and Mn-Fe SiO₂). This might be related to the absence of a targeting ligand on the particle surface that may provide room for improvement in the cytotoxic effect. Nevertheless, greater effects were still observed for AT (+) configurations in

apoptosis assay with a higher early apoptosis in the EMT6R cells in the order of free DOX < DOX@Mn-Fe CaCO₃ < DOX@Mn-Fe SiO₂ < DOX@Mn-Fe CaCO₃ (AT) < DOX@Mn-Fe SiO₂ (AT) (Figure 5D).

The internalization was examined by determining the endocytosis mechanism (Mn-Fe SiO₂ (AT) nanoagent) by applying three chemical inhibitors, cytochalasin D (phagocytic and macropinocytosis inhibitor; inhibitor 1), methyl- β -cyclodextrin (caveolin-mediated endocytosis inhibitor; inhibitor 2), and chlorpromazine hydrochloride (clathrin-mediated endocytosis inhibitor; inhibitor 3). Compared to inhibitor non-

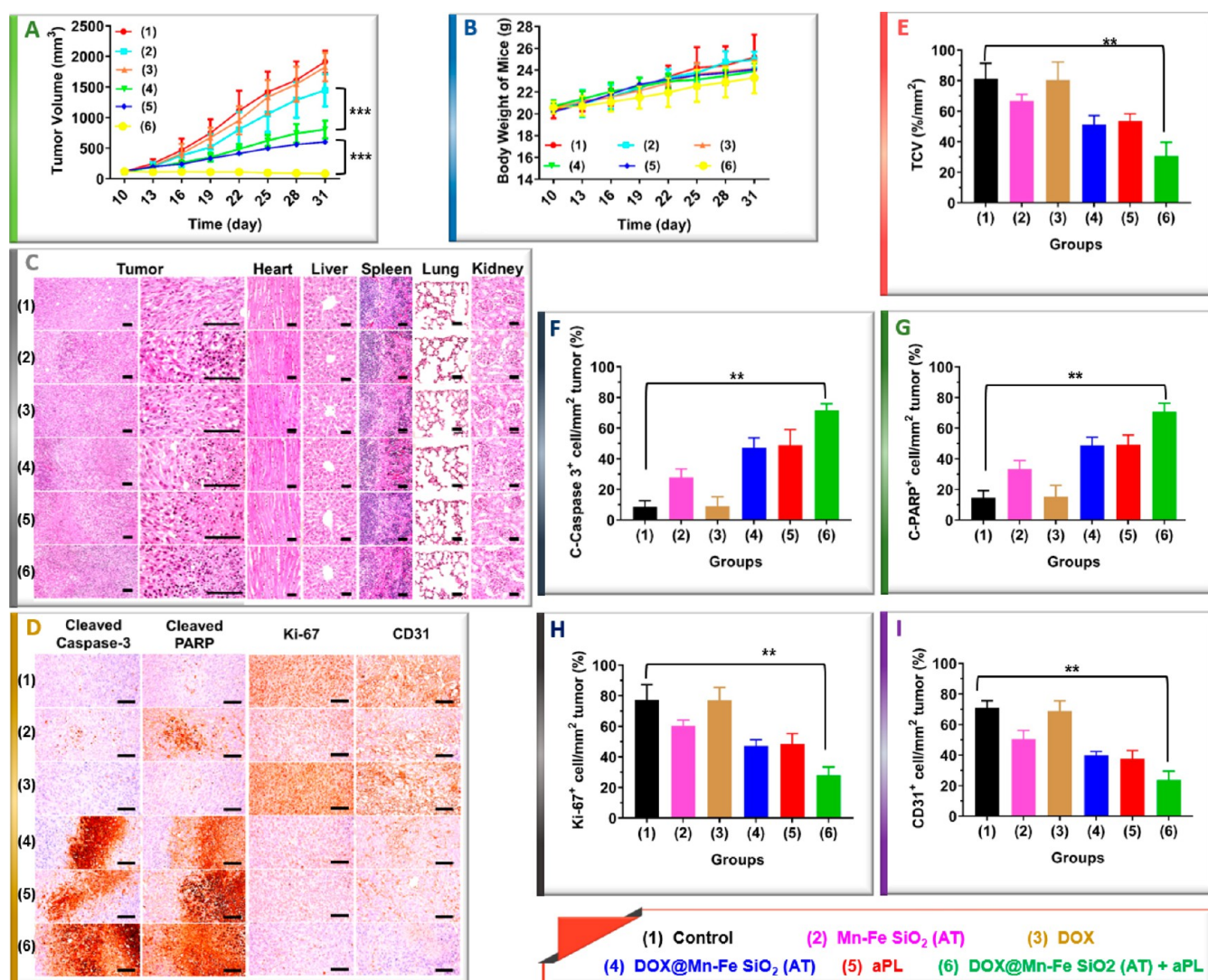


Figure 7. *In vivo* antitumor and biosafety study. The treatment groups are (1) control, (2) Mn-Fe SiO₂ (AT), (3) DOX, (4) DOX@Mn-Fe SiO₂ (AT), (5) aPL, and (6) DOX@Mn-Fe SiO₂ (AT) + aPL. (A, B) Tumor volume and body weight growth profiles from 21 days of monitoring. (C) HE staining images of tumors and vital organs (heart, liver, spleen, lung, and kidney) excised from the treatment groups (scale bars, 120 μ m). (D–I) Immunohistochemical examination with HE staining of TCV, cleaved-caspase-3, cleaved-PARP, Ki-67, and CD31 in tumor masses isolated after the treatments (scale bars, 120 μ m). ** p < 0.01.

treated hypoxic and resistant cells (no inhibitor), inhibitors 2 and 3 exhibited relatively small changes in internalization (Figure 6A). Inhibitor 1 showed the largest reduction in the internalization which was comparable to low-temperature-based uptake (denoted as low tem). These findings suggest that the nanoagent was internalized into the cells through micropinocytosis, phagocytosis, and caveolae-mediated endocytosis, owing to its surface spikes (Figure S10A,B). The issues at low pH and lysosomal degradation associated with the clathrin-mediated endocytosis might be evaded by the nanoagent following other pathways. On the other hand, this might make the interaction of macrophages with nanoparticles challenging and provide long-term systemic circulation.⁷⁴ Therefore, with the higher degree of internalization through multiple endocytic pathways and the higher rate of invasion with spiky exteriors, an *in vitro* spheroid penetration assay was conducted to confirm the penetration. Similar to the internalization, higher penetration activities were observed in the nanoagents (Figure 6B). Mn-Fe SiO₂ (AT) showed the

highest activity because of its more distinct spiky exteriors, making it the best candidate for *in vivo* models with deep tumor anticancer studies. The *in vivo* biodistribution assay was executed after developing a subcutaneous xenograft EMT6R tumor model with the systemic administration of cyanine 5.5 (Cy5.5; as a fluorescent probe) laden nanoagent and composite precursor particles. The acquisition of *in vivo* distribution images of Cy5.5 laden particles was performed for 24 h, and *ex vivo* imaging of excised tumors and vital organs (heart, lung, liver, kidney, spleen, and tumor) was conducted after 24 h of systemic administration. The resulting contours showed that the Cy5.5 laden nanoagents were retained in the encircled tumor region even after 12 h of the administration, whereas no significant fluorescence was observed after administrating the Cy5.5 laden composite precursors (Figure 6C). In particular, Cy5.5@Mn-Fe SiO₂ (AT) exhibited intense fluorescence in the tumor region 24 h postinjection, which matched the *ex vivo* imaging results and quantified plots (Figure 6D). These findings might be due to the higher

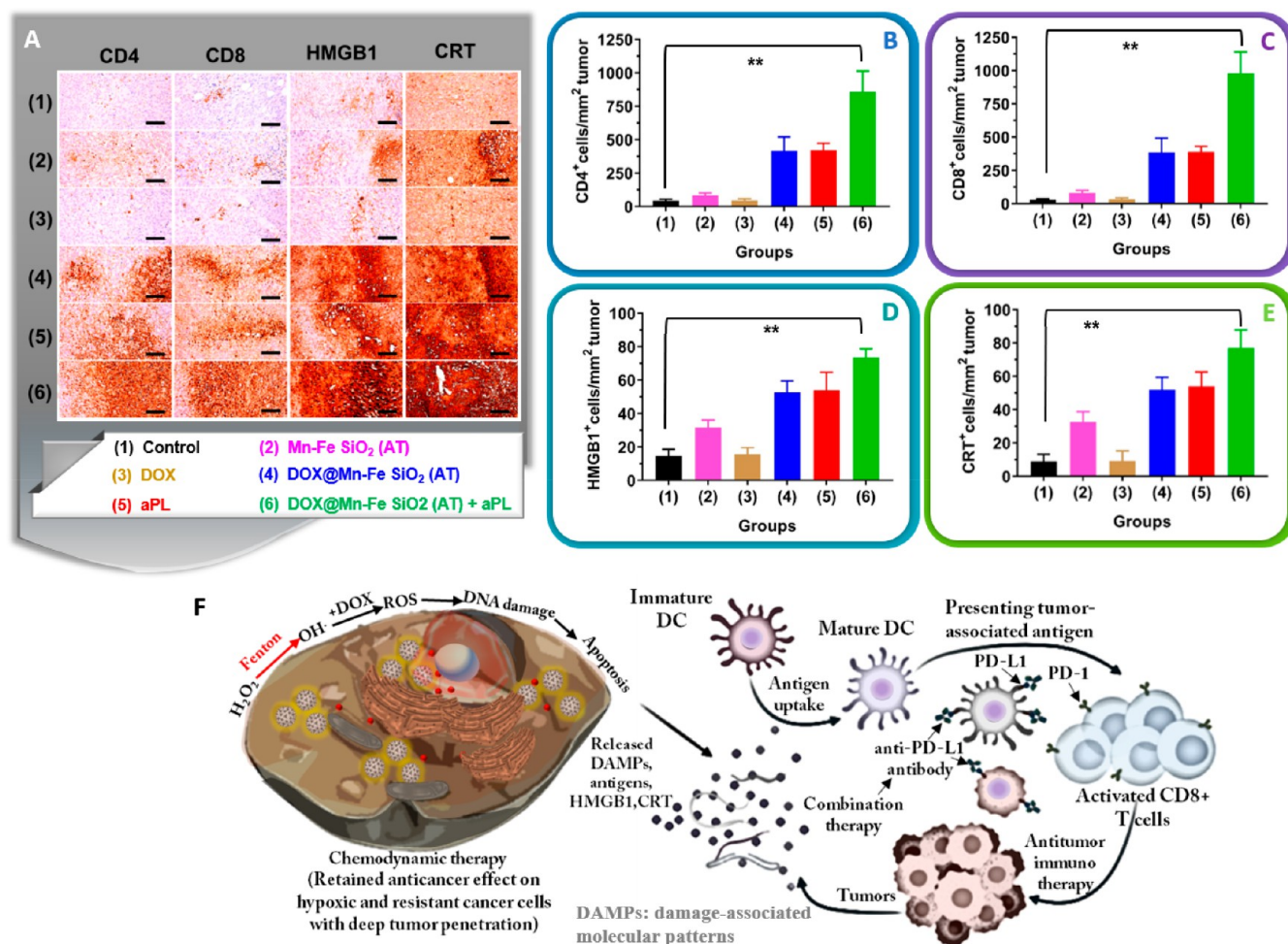


Figure 8. Immune cell examination and illustration of the plausible mechanistic model. The treatment groups are (1) control, (2) Mn–Fe SiO₂ (AT), (3) DOX, (4) DOX@Mn–Fe SiO₂ (AT), (5) aPL, and (6) DOX@Mn–Fe SiO₂ (AT) + aPL. (A–E) Immunohistochemical images and quantified plots for CD4, CD8, HMGB1, and CRT in the tumor masses harvested after the treatments (scale bars, 120 μ m). ** p < 0.01. (F) A plausible mechanistic model for the reinforced chemodynamic cancer therapy from DOX@Mn–Fe SiO₂ (AT) that induced chemodynamic therapy with ICD. DOX@Mn–Fe SiO₂ (AT) may be internalized into the tumor cells through phagocytosis, micropinocytosis, and caveolin-mediated endocytosis to release DOX for a chemo–chemodynamic effect with ICD. The apoptotic tumor cells may release HMGB1 and CRT that drive dendritic cell (DC) maturation and CD8⁺ T cell activation. Adding ICB aPL (i.e., DOX@Mn–Fe SiO₂ (AT) + aPL) may enhance the therapeutic efficacy from further reinforcement as chemo-immuno-chemodynamic therapy.

internalization and subsequent deep tumor penetration. The deposition in the heart, lung, and liver was the lowest after the Cy5.5@Mn–Fe SiO₂ (AT) treatment, whereas high accumulation levels were observed in the kidney and spleen compared to other configurations. This suggests that surface modification with targeting moieties might be necessary, even for spiky nanoagents to maximize the treatment efficacy with minimal off-target effects in normal tissues.

The increases in tumor volume and body weight of the treated mice were monitored to assess the *in vivo* biosafety. Immunogenic cell death (ICD) is also a combinable effect in conjunction with DOX to reinforce chemodynamic therapy. Thus, aPL was added to build DOX@Mn–Fe SiO₂ (AT) + aPL for chemo-immuno-chemodynamic anticancer therapeutics. EMT6R tumor-bearing mice were administered Mn–Fe SiO₂ (AT), free DOX, DOX@Mn–Fe SiO₂ (AT), aPL, and DOX@Mn–Fe SiO₂ (AT) + aPL. The Mn–Fe SiO₂ (AT) nanoagent was selected for the *in vivo* antitumor study because of the superior *in vitro* anticancer efficacy and the highest *in vivo* tumor accumulation. The suppression of tumor growth

was lowest for free DOX treatment (group 3) because of DOX resistance (Figure 7A). On the other hand, no significant fluctuations in body weight growth were observed (representing the compatibility of the dose and constituents selected for the study) in the treated mice (1–6) throughout the study period (Figure 7B). Mn–Fe SiO₂ (AT) nanoagent (group 2) treated mice showed better antitumor efficacy than that of free DOX due likely to the chemodynamic effect with enhanced internalization, which was further improved (comparable to aPL (group 5)) after DOX incorporation with Mn–Fe SiO₂ (AT) and DOX@Mn–Fe SiO₂ (AT) (group 4), because of the chemo (elevating the intracellular hydrogen peroxide level)^{75,76}-chemodynamic combination effect (transforming the elevated hydrogen peroxide to hydroxyl radicals).⁷⁷ After adding aPL to DOX@Mn–Fe SiO₂ (AT), DOX@Mn–Fe SiO₂ (AT) + aPL (group 6), no noticeable tumor growth (highest antitumor efficacy) was observed throughout the study period, which may be due to the chemo-immuno-chemodynamic combined effect. The biocompatibility was also assessed through histopathological image analysis. Similarly, no

significant damage was observed in histopathological observations of the major organs (heart, liver, spleen, lung, and kidney), proving that the nanoagent and analogs have no fatal toxicity in the *in vivo* model (Figure 7C). The cleaved caspase-3 and polyadenosine diphosphate-ribose polymerase (PARP) (apoptotic markers) and K_i -67 and CD31 (proliferation and angiogenesis markers) were examined from the treated tumor sections after the study (Figure 7D) with an estimation of the tumor cell volumes of the treated groups (Figure 7E). The expression levels of cleaved caspase-3 (Figure 7F) and PARP (Figure 7G) were the highest for the DOX@Mn–Fe SiO₂ (AT) + aPL treated groups (6). Correspondingly, those of K_i -67 (Figure 7H) and CD31 (Figure 7I) were the lowest for group 6, matching the order of tumor growth inhibition.

Immunomodulation was assessed by estimating the expression levels of the effector T cells (CD4⁺ and CD8⁺) and hallmarks of ICD (high mobility group box 1 (HMGB1⁺) and calreticulin (CRT⁺)) (Figure 8A). The combined configurations, DOX@Mn–Fe SiO₂ (AT) and DOX@Mn–Fe SiO₂ (AT) + aPL, exhibited comparable and superior levels (while significantly higher than the free DOX and Mn–Fe SiO₂ (AT) nanoagent alone) of intratumor CD4 (Figure 8B) and CD8 (Figure 8C) as well as higher levels of HMGB1 (Figure 8D; as activation of innate immunity) and CRT (Figure 8E; as a phagocytic marker in tumor mass) immunoreactive cells to aPL alone, respectively. These findings suggest that HMGB1 modulation and CRT upregulation can mediate the increased intratumor innate immunities and phagocytosis against tumor cells, respectively. The higher levels of Mn–Fe SiO₂ (AT) nanoagent than free DOX show that the nanoagent can generate an immune response for immunomodulation through ICD. DOX-loaded Mn–Fe SiO₂ (AT) evaded the drug resistance and potentiated the immune effects through the enhanced ICD via chemodynamic therapy with ROS-induced apoptosis (Figure 8F). The chemo-immuno-chemodynamic effect from the further addition of aPL to DOX@Mn–Fe SiO₂ (AT) acted against the immunosuppressive environment potentiating ICD by infiltrating cytotoxic T cells. The significant enhancement compared to aPL alone and DOX@Mn–Fe SiO₂ (AT) might be due to the spiky surface because the antibody specificity and avidity to tumor cells can be enhanced by loading the surface of anisotropic particles.⁷⁸ According to these outcomes, the incorporation of modified AT-manufactured Mn–Fe SiO₂ (AT) with DOX and aPL may be a promising and convenient treatment for resistant and solid (nonpenetrative, deep-seated) tumors only through the codelivery of chemotherapeutic agents and ICBs, even in the absence of targeting ligands and external stimuli.

The production costs were determined and compared by considering the necessary expenses (chemicals, feedstock, electricity, equipment, and others to manufacture 1 kg of product)⁷⁹ between the modified aerotaxy and conventional hydrothermal processes. The total costs for composite precursor particles and aerotaxied nanoagents were 682 and 954 USD, respectively. The cost increase was generated from additional electricity and aerotaxy equipment to produce Mn–Fe CaCO₃ (AT) and Mn–Fe SiO₂ (AT). On the other hand, the costs to produce analogous Mn–Fe CaCO₃ and Mn–Fe SiO₂ nanostructures using hydrothermal processes with separations and purifications⁸⁰ reached 1563 and 1548 USD, respectively. Unlike conventional hydrothermal reactions (Table S1), additional processes and pre/posttreatments were not required to replace the core nanobeads to proceed

with the different aerotaxies. Changing the line of suspension feedstock for the nanobeads was required to form different Mn–Fe nanoagents. This suggests that the modified aerotaxy proposed in this study could have actual competitive advantage in practical implementations despite the requirement for scale-up testing and surface modification of the nanoagents for optimal use in anticancer therapy.

CONCLUSIONS

A modified AT for the continuous plug-in assembly of the cell-penetrating Fenton nanoagents was used to reinforce chemodynamic cancer therapy. The in-flight epitaxial growth of Mn–Fe agglomerates (spark plasma between Mn and Fe rods) on amorphous CaCO₃ or SiO₂ nanobeads (mechanical spray of the nanobead suspension) at a high temperature (heated tube reactor) in the presence of sheath air flow allowed the convenience of the MnFe₂O₄ formation with a roughened (spiky) surface in a single-pass, waste-free configuration, which was unlike that observed conventional templated- or seed-mediated hydrothermal reactions to build anisotropic nanomaterials. The internalization and ROS generation activities of the resulting nanoagents were examined and compared with the composite precursors (Mn–Fe CaCO₃ or SiO₂ before AT) both under normoxic and hypoxic conditions to determine the effectiveness of AT in the cellular uptake and Fenton reaction-induced cancer cell apoptosis initiated by the preferential contact mode between the spiky surface and cell membrane. DOX was loaded on the AT assembled nanoagents and composite precursors and incubated with EMT6 and EMT6R (DOX-resistant) cells to identify and compare the overcoming levels of DOX resistance. The enhanced internalization activity of the nanoagents enabled combination (chemo-chemodynamic) anticancer effects, even for EMT6R cells, suggesting the versatility of the nanoagents that can be applied to a variety of microenvironments for combination chemodynamic cancer therapies. The loading of ICB aPL on DOX@Mn–Fe SiO₂ (AT) further enhanced the antitumor effect in an *in vivo* model despite the absence of targeting ligands and external stimuli. The modified AT introduced in this study provides another potential application of AT from the waste-free continuous manufacture of the Fenton-type nanoroughness on a nanobead for reinforcing chemodynamic cancer therapy while retaining biosafety. In addition, it can act as a plug-in dispenser capable of modularity and digitalization to be connected with artificial intelligence and machine learning platforms for smart nanotherapeutics.

METHODS

Fenton Nanoagent Manufacture and Characterization.

Mn–Fe agglomerates from a spark plasma (3 kV, 1 kHz) and amorphous CaCO₃ (or SiO₂) nanobeads from a mechanical spray (0.3 MPa) were combined serially at an orifice (0.5 mm, hole diameter) under nitrogen gas flow (2 l/min) and injected into a heated tube reactor (wall temperature of 1050 °C) with sheath air flow (1 l/min). In the tube reactor, epitaxial growth with oxidation of the Mn–Fe on the nanobeads enabled the formation of spiky MnFe₂O₄ in a single-pass in-flight configuration. The part of the resulting particle-laden flow was sampled directly to obtain the aerosol size distribution, and the data were acquired using an SMPS (3936, TSI, USA). The resulting particles collected on a polytetrafluoroethylene membrane filter were dispersed in PBS under bath sonication to measure the DLS size distribution and zeta potential using a Nano-S90 ZetaSizer (Malvern Instruments, UK). Aerosol charge current levels were obtained using an aerosol electrometer

(Charme, Palas, Germany) to examine electrostatic states of the resulting particle surface. The shape and microstructure of the resulting particles were observed by TEM (Tecnai G2 F20 S-TWIN, FEI, USA) after placing the resulting particles on carbon-coated copper grids (Ted Pella, Inc., USA) using a mini-particle sampler (Ecomasure, France). The crystallinity and surface state were analyzed by XRD (X'Pert3MRD, Panalytical, UK) and XPS (K-Alpha, Thermo Scientific, USA), respectively. The textural properties of the amorphous nanobeads as supporting particles were obtained using a porosimeter (ASAP 2010, Micromeritics, USA) to identify the adsorption–desorption isotherms in relation to specific surface areas and average pore diameters.

Transfection Ability. EMT6 cells were exposed to pDNA-loaded nanoagents (nanoagent to pDNA, 10:1; *w/w*) in the absence and presence of PEI (prepared by immersion of 25 μg of nanoagent in 1 mL of PEI solution (PEI Prime, Serochem, USA)) for 4 h at 37 °C. Transfection efficiency (expressed as relative luminescence unit (RLU)/mg of protein) was obtained using a luminometer (TD-20/20, Promega, USA).

Hemolysis. The hemotoxicity of the resulting particles from the individual plug-in operations was examined as a prescreening process to optimize the AT conditions. The whole blood was withdrawn from BALB/c mice and centrifuged (500 \times g, 10 min) for plasma removal before conducting a hemolysis assay with erythrocyte suspension. The erythrocytes suspension (1 mL) was mixed with 8 mL of normal saline and 1 mL of the resulting particles (500 $\mu\text{g}/\text{mL}$) before and after AT. The erythrocytes dispersed with deionized water and PBS were used as a positive and negative control, respectively. After shaking incubation (100 rpm, 37 °C) for 8 h, the erythrocytes were centrifuged. The hemolytic percentage of the particles was estimated by UV–Vis spectrophotometry (U-2800, PerkinElmer, USA) at 540 nm by calculating the hemoglobin content in the supernatant of the suspension.

LC, EE, and In Vitro DOX Release. The DOX loaded in the resulting nanoagents (Mn–Fe CaCO_3 (AT) and Mn–Fe SiO_2 (AT)), and composite precursors (Mn–Fe CaCO_3 and Mn–Fe SiO_2) was elucidated by separating DOX from the DOX loaded formulations using a centrifugal ultrafiltration device (Amicon, MWCO 10000 Da, Millipore, USA) at 5000 rpm for 10 min. The concentration of DOX was determined using a UV–vis spectrophotometer at 485 nm. The LC and EE were estimated using the following formula:

$$EE (\%) = W_{\text{EDOX}}/W_{\text{TDOX}} \times 100$$

$$LC (\%) = W_{\text{TDOX}} - W_{\text{UDOX}}/W_{\text{TF}} \times 100$$

where W_{EDOX} , W_{TDOX} , W_{UDOX} , and W_{TF} are the weights of the entrapped DOX in the formulations, total DOX, unbound DOX, and total formulations, respectively. The *in vitro* release profiles of DOX from DOX-loaded nanoagents and composite precursors at pH 6.5 and 7.4 were acquired in a shaking incubator (100 rpm, 37 °C) after dispersal in PBS. One milliliter of each suspension was enclosed in a dialysis bag (MWCO = 3500 Da) and immersed in 25 mL of PBS (pH 6.5 and 7.4). The DOX released in the medium was measured at predetermined times using a UV–vis spectrophotometer at 485 nm.

Cells. A murine mammary carcinoma cell line (EMT6) was cultured in Dulbecco's high-glucose modified Eagle's medium (DMEM; GE Healthcare Life Sciences, USA) accompanied by fetal bovine serum (FBS, 10%), penicillin G sodium (100 U/mL), and streptomycin sulfate (100 $\mu\text{g}/\text{mL}$) in an incubator (37 °C, 5% CO_2). EMT6R cells were developed according to previous reports.^{81,82} For the development of hypoxic EMT6 cells, the cells were placed in an anaerobic hypoxic chamber with 94% N_2 , 5% CO_2 , and 1% O_2 .^{83,84} CD8^+ T cells were isolated from the spleen of the BALB/c mouse from EasySep™ Mouse Naïve CD8^+ T cell Isolation Kit, as reported in a previous study.⁸²

Cellular Uptake. Twenty-four hours before treatment, EMT6 cells (2×10^5 cells/well) were cultured on 12-well plates for adhesion. The cells were treated with coumarin-6 (1 $\mu\text{g}/\text{mL}$)-loaded nanoagents and composite precursors (25 $\mu\text{g}/\text{mL}$) for 2 h at 37 °C. The cells were harvested after 2 h, washed twice with PBS, and examined

by flow cytometry. The cellular uptake mechanism was analyzed by culturing EMT6 cells (2×10^5 cells/well) on 12-well plates for 24 h for adhesion. Before treatment with the nanoagents and composite precursors (25 $\mu\text{g}/\text{mL}$), the EMT6 cells were pretreated with cytochalasin D (4 μM , phagocytosis and macro-pinocytosis inhibitor; PHZ1063, Invitrogen, USA), chlorpromazine hydrochloride (100 μM , clathrin-mediated endocytosis inhibitor; C8138, Sigma-Aldrich, USA), or methyl- β -cyclodextrin (10 mM, caveolin-mediated endocytosis inhibitor; C4555, Sigma-Aldrich, USA) for 1 h at 4 °C. After 2 h of treatment, the cells were harvested, washed with PBS, and analyzed by flow cytometry.

In Vitro Cytotoxicity. Each well of a 96-well plate was seeded with 5×10^3 EMT6 cells, incubated for 24 h, and treated with the nanoagents and composite precursors for 24 h. The treated cells were then washed with PBS and incubated for 6 h with 50 μL (2.5 mg/mL) of an MTT solution (Sigma-Aldrich, USA). The formazan crystals were dissolved in 100 μL dimethyl sulfoxide, and the absorbance was measured using a microplate reader (Thermo Scientific, USA) at 570 nm.

In Vitro ROS Generation. EMT6 cells (2×10^5 cells/well) were cultured on a 12-well plate, incubated for 24 h, and treated with the nanoagents and composite precursors for 24 h. The cells were incubated with DCFDA (green fluorescence) for 1 h, washed with PBS, and trypsinized, harvested, and resuspended for flow cytometry. The levels of ROS in the treated cells were determined by measuring the green fluorescence.

Atomic Absorption Spectroscopy. The release of Mn (279.5 nm in wavelength) and Fe (248.3 nm) ions at pH 6.5 was detected. The resulting nanoagents (1 mg) were dispersed in 1 mL of buffered saline (pH 6.5, 37 °C) for 48 h. The dispersion was centrifuged, filtered, diluted with deionized water, and transferred for spectroscopy (iCE 3300, Thermo Scientific, USA).

Apoptosis. EMT6 cells (2×10^5 cells/well) were cultured on a 12-well plate, incubated for 16 h, and treated with the nanoagents and composite precursors for 48 h. The cells were washed three times with PBS, trypsinized, resuspended in binding buffer containing Annexin V-FITC and PI, incubated for 15 min in the dark, and resuspended in PBS for flow cytometry.

In Vitro Tumor Spheroid Penetration. For the development of the solid EMT6 spheroid model, EMT6 cells (1×10^3 cells/well) were seeded in 96-well plates (precoated with low-melting-temperature agarose (2%)) and cultured for 15 days (media was refreshed every 2 days). The spheroids were seeded onto 12-well plates and exposed to coumarin-6 (1 $\mu\text{g}/\text{mL}$)-loaded nanoagents and composite precursors for 12 h. The spheroids were washed three times with PBS, placed on fresh media, and imaged by fluorescence microscopy (Eclipse Ti, Nikon Instruments, Japan).

Biodistribution. The nanoagents and composite precursors were injected intravenously into EMT6R xenograft-bearing BALB/c mice after tagging Cy5.5 (1 $\mu\text{g}/\text{mL}$) for fluorescence-based *in vivo* and *ex vivo* imaging. The fluorescence-labeled organism bioimaging (FOBI, Neoscience, Korea) system was used to image the treated mice and extracted organs. At predetermined time points for 24 h, the treated mice were imaged, and the Cy5.5 distributions were recorded. *Ex vivo* imaging was conducted after the mice were sacrificed by CO_2 asphyxiation, and the tumors and principal organs were isolated. The organs and tumors were positioned in the imaging system, and the fluorescence intensities were calculated using NEO imaging software.

Histopathology. The principal organs (heart, lung, liver, kidney, and spleen) and tumors from the treatments with free DOX, Mn–Fe SiO_2 (AT), DOX@Mn–Fe SiO_2 (AT), free aPL, and DOX@Mn–Fe SiO_2 (AT) + aPL were harvested from the sacrificed mice, sliced (3–4 μm), embedded in paraffin, and stained with HE for analysis using an optical microscope (Eclipse 80i, Nikon, Japan).

In Vivo Antitumor Study. After a subcutaneous injection of EMT6R cells (1×10^6), EMT6R xenograft tumors were established in five-week-old female BALB/c nude mice. The mice were distributed into six groups (six mice per group) after the tumor volume reached $\sim 100 \text{ mm}^3$ and treated with free DOX, Mn–Fe SiO_2 (AT), DOX@

Mn–Fe SiO₂ (AT), free aPL, and DOX@Mn–Fe SiO₂ (AT) + aPL. Free DOX was injected for comparison at an equivalent dose (0.5 mg/kg). The tumor volumes were assessed using the formula ($1/2 \times \text{longest dimension} \times \text{shortest dimension}^2$). A set of Vernier calipers was used to measure the dimensions.

Immunohistochemistry. The tumors from the treated mice were excised and sliced to assess the expression of the tumor cell proliferation marker (Ki-67), angiogenesis marker (CD31), and apoptotic markers (cleaved caspase-3 and cleaved PARP). The immunoreactivity fluctuations in the tumor masses were examined using purified primary antibodies against HMGB1, CRT, CD4, and CD8 with a peroxidase substrate kit (Vector Laboratories, Burlingame, USA) and avidin–biotin–peroxidase complex. To be identified as positive, there should be more than 20% occupation of the tissues from the immunoreactivities of each marker. The coverage of HMGB1- and CRT-positive cells on the tumor regions (%/mm² of the tumor mass) and the mean number of CD4 and CD8 immunolabeled cells infiltrated into the tumor masses (cells/mm² of tumor mass) were evaluated using automated image analysis, as described elsewhere.^{85,86}

All mice experiments were approved and followed the instructions and guidelines of the Institutional Animal Ethics Committee, Yeungnam University, Republic of Korea. The measurements were performed with the mean \pm SD. The statistical significance between the groups was evaluated using a Student's *t*-test and one-way analysis of variance; *p* values < 0.05 were considered significant.

ASSOCIATED CONTENT

Supporting Information

The Supporting Information is available free of charge at <https://pubs.acs.org/doi/10.1021/acsnano.2c09136>.

Schematics of plug-in aerotaxy and subsequent DOX and aPL loading; hemolysis assay results of nanoagents and composite precursors; particle size distributions for aerosol state and aqueous dispersion, including zeta potential and aerosol charge current of resulting nanoagents; low- and high-magnification TEM images of individual Mn–Fe agglomerates and core nanobeads; adsorption–desorption isotherms of nanobeads, including specific surface area and average pore diameter; XRD profiles and surface states of nanoagents after aerotaxy, including transfection results with and without PEI; CD8 cocultured cell viabilities treated with nanoagents; viabilities and Western blots of EMT6 and EMT6R cells treated with different DOX concentrations; EE, LC, and DOX release profiles of nanoagents; mechanistic schemes for cellular internalization nanoagents (PDF)

AUTHOR INFORMATION

Corresponding Authors

Jungho Hwang — School of Mechanical Engineering, Yonsei University, Seoul 03722, Republic of Korea; orcid.org/0000-0002-0304-7360; Email: hwangjh@yonsei.ac.kr

Jong Oh Kim — College of Pharmacy, Yeungnam University, Gyeongsan 38541, Republic of Korea; orcid.org/0000-0002-4929-851X; Email: jongohkim@yu.ac.kr

Jeong Hoon Byeon — School of Mechanical Engineering, Yeungnam University, Gyeongsan 38541, Republic of Korea; orcid.org/0000-0003-0903-7128; Email: postjb@yu.ac.kr

Authors

Kishwor Poudel — College of Pharmacy, Yeungnam University, Gyeongsan 38541, Republic of Korea; Wellman Center for Photomedicine, Department of Dermatology,

Massachusetts General Hospital, Harvard Medical School, Boston, Massachusetts 02114, United States

Kang Sik Nam — School of Mechanical Engineering, Yonsei University, Seoul 03722, Republic of Korea

Jiseok Lim — School of Mechanical Engineering, Yeungnam University, Gyeongsan 38541, Republic of Korea

Sae Kwang Ku — College of Korean Medicine, Daegu Haany University, Gyeongsan 38610, Republic of Korea

Complete contact information is available at:

<https://pubs.acs.org/doi/10.1021/acsnano.2c09136>

Author Contributions

*K.P., K.S.N., and J.L. contributed equally to this work.

Notes

The authors declare no competing financial interest.

ACKNOWLEDGMENTS

This research was supported by the National Research Foundation of Korea (NRF) funded by the Ministry of Science, ICT and future Planning (Nos. 2022R1A2C1009389, 2021R1A6A1A03039493, and 2021R1A2C3009556). This work was also supported by Korea Environment Industry & Technology Institute (KEITI) through Technology Development Project for Biological Hazards Management in Indoor Air Program, funded by Korea Ministry of Environment (MOE) (2021003370005) and the Research Grant of Yeungnam University, Republic of Korea (219A380028).

REFERENCES

- (1) Bruun, T. U. J.; Andersson, A.-M. C.; Draper, S. J.; Howarth, M. Engineering a Rugged Nanoscaffold to Enhance Plug-and-Display Vaccination. *ACS Nano* **2018**, *12*, 8855–8866.
- (2) Suh, S.; Jo, A.; Traore, M. A.; Zhan, Y.; Coutermarsh-Ott, S. L.; Ringel-Scalia, V. M.; Allen, I. C.; Davis, R. M.; Behkam, B. Nanoscale Bacteria-Enabled Drug Delivery System (NanoBEADS) Enhances Intratumoral Transport of Nanomedicine. *Adv. Sci.* **2019**, *6*, 1801309.
- (3) Xu, B.; Cui, Y.; Wang, W.; Li, S.; Lyu, C.; Wang, S.; Bao, W.; Wang, H.; Qin, M.; Liu, Z.; Wei, W.; Liu, H. Immunomodulation-Enhanced Nanozyme-Based Tumor Catalytic Therapy. *Adv. Mater.* **2020**, *32*, 2003563.
- (4) Zhu, X.; Vo, C.; Taylor, M.; Smith, B. R. Non-Spherical Micro- and Nanoparticles in Nanomedicine. *Mater. Horiz.* **2019**, *6*, 1094–1121.
- (5) Sun, Y.; Yan, C.; Xie, J.; Yan, D.; Hu, K.; Huang, S.; Liu, J.; Zhang, Y.; Gu, N.; Xiong, F. High-Performance Work-like Mn-Zn Ferrite Theranostic Nanoagents and the Application on Tumor Theranostics. *ACS Appl. Mater. Interfaces* **2019**, *11*, 29536–29548.
- (6) Yan, R.; Chen, J.; Wang, J.; Rao, J.; Du, X.; Liu, Y.; Zhang, L.; Qiu, L.; Liu, B.; Zhao, Y.-D.; Jiang, P.; Chen, C.; Li, Y.-Q. A NanoFlare-Based Strategy for *In Situ* Tumor Margin Demarcation and Neoadjuvant Gene/Photothermal Therapy. *Small* **2018**, *14*, 1802745.
- (7) Truong, N. P.; Whittaker, M. R.; Mak, C. W.; Davis, T. P. The Importance of Nanoparticle Shape in Cancer Drug Delivery. *Expert Opin. Drug Delivery* **2015**, *12*, 129–142.
- (8) Zhang, J.; Wang, Z.; Gao, Y.; Wu, Z.-S. Simple Self-Assembled Targeting DNA Nano Sea Urchin as a Multivalent Drug Carrier. *ACS Appl. Bio Mater.* **2020**, *3*, 4514–4521.
- (9) Wang, W.; Wang, P.; Tang, T.; Elzatahry, A. A.; Wang, S.; Al-Dahyan, D.; Zhao, M.; Yao, C.; Hung, C.-T.; Zhu, X.; Zhao, T.; Li, X.; Zhang, F.; Zhao, D. Facile Synthesis of Uniform Virus-like Mesoporous Silica Nanoparticles for Enhanced Cellular Internalization. *ACS Cent. Sci.* **2017**, *3*, 839–846.
- (10) Fu, J.; An, D.; Song, Y.; Wang, C.; Qiu, M.; Zhang, H. Janus Nanoparticles for Cellular Delivery Chemotherapy: Recent Advances and Challenges. *Coord. Chem. Rev.* **2020**, *422*, 213467.

- (11) Zhao, L.; Song, X.; Ouyang, X.; Zhou, J.; Li, J.; Deng, D. Bioinspired Virus-like Fe₃O₄/Au@C Nanovector for Programmable Drug Delivery via Hierarchical Targeting. *ACS Appl. Mater. Interfaces* **2021**, *13*, 49631–49641.
- (12) Chen, J.; Clay, N. E.; Park, N.-h.; Kong, H. Non-Spherical Particles for Targeted Drug Delivery. *Chem. Eng. Sci.* **2015**, *125*, 20–24.
- (13) Lee, S.-Y.; Ferrari, M.; Decuzzi, P. Shaping Nano-/Micro-Particles for Enhanced Vascular Interaction in Laminar Flows. *Nanotechnology* **2009**, *20*, 49S101.
- (14) Nocito, G.; Petralia, S.; Malanga, M.; Béni, S.; Calabrese, G.; Parenti, R.; Conoci, S.; Sortino, S. Biofriendly Route to Near-Infrared-Active Gold Nanotriangles and Nanoflowers through Nitric Oxide Photorelease for Photothermal Applications. *ACS Appl. Nano Mater.* **2019**, *2*, 7916–7923.
- (15) Hayat, H.; Nukala, A.; Nyamira, A.; Fan, J.; Wang, P. A Concise Review: The Synergy between Artificial Intelligence and Biomedical Nanomaterials that Empowers Nanomedicine. *Biomed. Mater.* **2021**, *16*, 052001.
- (16) Seaberg, J.; Montazerian, H.; Hossen, M. N.; Bhattacharya, R.; Khademhosseini, A.; Mukherjee, P. Hybrid Nanosystems for Biomedical Applications. *ACS Nano* **2021**, *15*, 2099–2142.
- (17) Xu, M.; Song, Y.; Wang, J.; Li, N. Anisotropic Transition Metal-Based Nanomaterials for Biomedical Applications. *View* **2021**, *2*, 20200154.
- (18) Tang, Z.; Zhao, P.; Wang, H.; Liu, Y.; Bu, W. Biomedicine Meets Fenton Chemistry. *Chem. Rev.* **2021**, *121*, 1981–2019.
- (19) Herrmann, I. K.; Wood, M. J. A.; Fuhrmann, G. Extracellular Vesicles as a Next-Generation Drug Delivery Platform. *Nat. Nanotechnol.* **2021**, *16*, 748–759.
- (20) Falsini, S.; Bardi, U.; Abou-Hassan, A.; Ristori, S. Sustainable Strategies for Large-Scale Nanotechnology Manufacturing in the Biomedical Field. *Green Chem.* **2018**, *20*, 3897–3907.
- (21) Heurlin, M.; Magnusson, M. H.; Lindgren, D.; Ek, M.; Wallenberg, L. R.; Deppert, K.; Samuelson, L. Continuous Gas-Phase Synthesis of Nanowires with Tunable Properties. *Nature* **2012**, *492*, 90–94.
- (22) Metaferia, W.; Persson, A. R.; Mergenthaler, K.; Yang, F.; Zhang, W.; Yartsev, A.; Wallenberg, R.; Pistol, M.-E.; Deppert, K.; Samuelson, L.; Magnusson, M. H. GaAsP Nanowires Grown by Aerotaxy. *Nano Lett.* **2016**, *16*, 5701–5707.
- (23) Persson, A. R.; Metaferia, W.; Sivakumar, S.; Samuelson, L.; Magnusson, M. H.; Wallenberg, R. Electron Tomography Reveals the Droplet Covered Surface Structure of Nanowires Grown by Aerotaxy. *Small* **2018**, *14*, 1801285.
- (24) Barrigón, E.; Hultin, O.; Lindgren, D.; Yadegari, F.; Magnusson, M. H.; Samuelson, L.; Johansson, L. I. M.; Björk, M. T. GaAs Nanowire pn-Junctions Produced by Low-Cost and High-Throughput Aerotaxy. *Nano Lett.* **2018**, *18*, 1088–1092.
- (25) McKibbin, S. R.; Yngman, S.; Balmes, O.; Meuller, B. O.; Tågerud, S.; Messing, M. E.; Portale, G.; Sztucki, M.; Deppert, K.; Samuelson, L.; Magnusson, M. H.; Lundgren, E.; Mikkelsen, A. *In Situ* Observation of Synthesized Nanoparticles in Ultra-Dilute Aerosols via X-Ray Scattering. *Nano Res.* **2019**, *12*, 25–31.
- (26) Poudel, B. K.; Park, J. H.; Lim, J.; Byeon, J. H. Direct Fluorescent Labeling for Efficient Biological Assessment of Inhalable Particles. *Nanotoxicology* **2017**, *11*, 953–963.
- (27) Byeon, J. H.; Kim, Y.-W. Aero-Self-Assembly of Ultrafine Gold Incorporated Silica Nanobunches for NIR-Induced Chemo-Thermal Therapy. *Small* **2014**, *10*, 2331–2335.
- (28) Hong, J.; Murphy, A. B.; Ashford, B.; Cullen, P. J.; Belmonte, T.; Ostrikov, K. Plasma-Digital Nexus: Plasma Nanotechnology for the Digital Manufacturing Age. *Rev. Mod. Plasma Phys.* **2020**, *4*, 1.
- (29) Jung, W.; Jung, Y.-H.; Pikhitsa, P. V.; Feng, J.; Yang, Y.; Kim, M.; Tsai, H.-Y.; Tanaka, T.; Shin, J.; Kim, K.-Y.; Choi, H.; Rho, J.; Choi, M. Three-Dimensional Nanoprinting via Charged Aerosol Jets. *Nature* **2021**, *592*, 54–59.
- (30) Wang, X.; Sparkman, J.; Gou, J. Strain Sensing of Printed Carbon Nanotube Sensors on Polyurethane Substrate with Spray Deposition Modeling. *Compos. Commun.* **2017**, *3*, 1–6.
- (31) Fu, L.-H.; Wan, Y.; Qi, C.; He, J.; Li, C.; Yang, C.; Xu, H.; Lin, J.; Huang, P. Nanocatalytic Theranostics with Glutathione Depletion and Enhanced Reactive Oxygen Species Generation for Efficient Cancer Therapy. *Adv. Mater.* **2021**, *33*, 2006892.
- (32) Hu, H.; Feng, W.; Qian, X.; Yu, L.; Chen, Y.; Li, Y. Emerging Nanomedicine-Enabled Nanodynamic Therapies beyond Traditional Photodynamics. *Adv. Mater.* **2021**, *33*, 2005062.
- (33) Li, Y.; Xiu, W.; Yang, K.; Wen, Q.; Yuwen, L.; Luo, Z.; Liu, X.; Yang, D.; Xie, X.; Wang, L. A Multifunctional Fenton Nanoagent for Microenvironment-Selective Anti-Biofilm and Anti-Inflammatory Therapy. *Mater. Horiz.* **2021**, *8*, 1264–1271.
- (34) Li, S.-L.; Jiang, P.; Jiang, F.-L.; Liu, Y. Recent Advances in Nanomaterial-Based Nanoplatforms for Chemodynamic Cancer Therapy. *Adv. Funct. Mater.* **2021**, *31*, 2100243.
- (35) Jia, T.; Wang, Z.; Sun, Q.; Dong, S.; Xu, J.; Zhang, F.; Feng, L.; He, F.; Yang, D.; Yang, P.; Lin, J. Intelligent Fe-Mn Layered Double Hydroxides Nanosheets Anchored with Upconversion Nanoparticles for Oxygen-Elevated Synergetic Therapy and Bioimaging. *Small* **2020**, *16*, 2001343.
- (36) Tian, Q.; Xue, F.; Wang, Y.; Cheng, Y.; An, L.; Yang, S.; Chen, X.; Huang, G. Recent Advances in Enhanced Chemodynamic Therapy Strategies. *Nano Today* **2021**, *39*, 101162.
- (37) Sang, Y.; Cao, F.; Li, W.; Zhang, L.; You, Y.; Deng, Q.; Dong, K.; Ren, J.; Qu, X. Bioinspired Construction of a Nanozyme-Based H₂O₂ Homeostasis Disruptor for Intensive Chemodynamic Therapy. *J. Am. Chem. Soc.* **2020**, *142*, 5177–5183.
- (38) Jia, C.; Guo, Y.; Wu, F.-G. Chemodynamic Therapy via Fenton and Fenton-Like Nanomaterials: Strategies and Recent Advances. *Small* **2022**, *16*, 2103868.
- (39) Qiu, J.; Nguyen, Q. N.; Lyu, Z.; Wang, Q.; Xia, Y. Bimetallic Janus Nanocrystals: Syntheses and Applications. *Adv. Mater.* **2022**, *34*, 2102591.
- (40) Dong, Z.; Hao, Y.; Yang, Z.; Zhu, Y.; Liu, Z.; Feng, L. Metal-Polyphenol-Network Coated CaCO₃ as pH-Responsive Carriers to Enable Effective Intratumoral Penetration and Reversal of Multidrug Resistance for Augmented Cancer Treatments. *Nano Res.* **2020**, *13*, 3057–3067.
- (41) Jiang, H.; Guo, Y.; Wei, C.; Hu, P.; Shi, J. Nanocatalytic Innate Immunity Activation by Mitochondrial DNA Oxidative Damage for Tumor-Specific Therapy. *Adv. Mater.* **2021**, *33*, 2008065.
- (42) Wang, S.; Yu, G.; Wang, Z.; Jacobson, O.; Lin, L.-S.; Yang, W.; Deng, H.; He, Z.; Liu, Y.; Chen, Z.-Y.; Chen, X. Enhanced Antitumor Efficacy by a Cascade of Reactive Oxygen Species Generation and Drug Release. *Angew. Chem.* **2019**, *131*, 14900–14905.
- (43) Wang, X.; Zhong, X.; Liu, Z.; Cheng, L. Recent Progress of Chemodynamic Therapy-Induced Combination Cancer Therapy. *Nano Today* **2020**, *35*, 100946.
- (44) Fissan, H.; Ristig, S.; Kaminski, H.; Asbach, C.; Eppe, M. Comparison of Different Characterization Methods for Nanoparticle Dispersions Before and After Aerosolization. *Anal. Methods* **2014**, *6*, 7324–7334.
- (45) Danaei, M.; Dehghankhold, M.; Ataei, S.; Davarani, F. H.; Javanmard, R.; Dokhani, A.; Khorasani, S.; Mozafari, M. R. Impact of Particle Size and Polydispersity Index on the Clinical Applications of Lipidic Nanocarrier Systems. *Pharmaceutics* **2018**, *10*, 57.
- (46) Chen, M.; Liu, X.; Fahr, A. Skin Penetration and Deposition of Carboxyfluorescein and Temoporfin from Different Lipid Vesicular Systems: *In Vitro* Study with Finite and Infinite Dosage Application. *Int. J. Pharm.* **2011**, *408*, 223–234.
- (47) Cheng, K. L. The Negative Charge of Nanoparticles. *Microchem. J.* **2006**, *82*, 119–120.
- (48) Bondi, J. F.; Oyler, K. D.; Ke, X.; Schiffer, P.; Schaak, R. E. Chemical Synthesis of Air-Stable Manganese Nanoparticles. *J. Am. Chem. Soc.* **2009**, *131*, 9144–9145.
- (49) Kwak, B.; Choi, J.; Lim, J.; Byeon, J. H. Combining Plug-In Devices for Reconfigurable Removal of Trichloroethylene and Heavy

Metal Ion in Aqueous Solution: Application and Biosafety of Iron-Iron Sulfide and Its Composites. *J. Clean. Prod.* **2021**, *314*, 128069.

(50) Pal, M.; Rakshit, R.; Mandal, K. Surface Modification of MnFe_2O_4 Nanoparticles to Impart Intrinsic Multiple Fluorescence and Novel Photocatalytic Properties. *ACS Appl. Mater. Interfaces* **2014**, *6*, 4903–4910.

(51) Fahmi, M. Z.; Ou, K.-L.; Chen, J.-K.; Ho, M.-H.; Tzing, S.-H.; Chang, J.-Y. Development of Bovine Serum Albumin-Modified Hybrid Nanoclusters for Magnetofluorescence Imaging and Drug Delivery. *RSC Adv.* **2014**, *4*, 32762–32772.

(52) Xia, J.; Noguchi, Y.; Xu, X.; Odaira, T.; Kimura, Y.; Nagasako, M.; Omori, T.; Kainuma, R. Iron-Based Superelastic Alloys with Near-Constant Critical Stress Temperature Dependence. *Science* **2020**, *369*, 855–858.

(53) Sun, R.; Willhammar, T.; Grape, E. S.; Strømme, M.; Cheung, O. Mesoscale Transformation of Amorphous Calcium Carbonate to Porous Vaterite Microparticles with Morphology Control. *Cryst. Growth Des.* **2019**, *19*, S075–S087.

(54) Ke, X.; Wu, Z.; Lin, J.; Wang, F.; Li, P.; Xu, R.; Yang, M.; Han, L.; Zhang, D. A Rapid Analytical Method for the Specific Surface Area of Amorphous SiO_2 Based on X-Ray Diffraction. *J. Non-Cryst. Solids* **2020**, *531*, 119841.

(55) Iqbal, M. Z.; Ren, W.; Saeed, M.; Chen, T.; Ma, X.; Yu, X.; Zhang, J.; Zhang, L.; Li, A.; Wu, A. A Facile Fabrication Route for Binary Transition Metal Oxide-Based Janus Nanoparticles for Cancer Theranostic Applications. *Nano Res.* **2018**, *11*, 5735–5750.

(56) Byeon, J. H.; Hwang, J. Morphology of Metallic Nanoparticles as a Function of Deposition Time in Electroless Deposition of Metal on Multi-Walled Carbon Nanotubes. *Surf. Coat. Technol.* **2008**, *203*, 357–363.

(57) Gong, L.; Chen, G.; Lv, J.; Lu, M.; Zhang, J.; Wu, X.; Wang, J. Phase Transition-Enabled MnFe_2O_4 Nanoparticles Modulated by High-Pressure with Enhanced Electrical Transport Properties. *Appl. Surf. Sci.* **2021**, *565*, 150532.

(58) Ma, Y.; Xu, X.; Lu, L.; Meng, K.; Wu, Y.; Chen, J.; Miao, J.; Jiang, Y. Facile Synthesis of Ultrasmall MnFe_2O_4 Nanoparticles with High Saturation Magnetization for Magnetic Resonance Imaging. *Ceram. Int.* **2021**, *47*, 34005–34011.

(59) Thahir, R.; Wahab, A. W.; Nafie, N. L.; Raya, I. Synthesis of High Surface Area Mesoporous Silica SBA-15 by Adjusting Hydrothermal Treatment Time and the Amount of Polyvinyl Alcohol. *Open Chem.* **2019**, *17*, 963–971.

(60) Xiang, L.; Kong, W.; Su, J.; Liang, J.; Zhang, G.; Xie, L.; Zhang, R. Amorphous Calcium Carbonate Precipitation by Cellular Biomineralization in Mantle Cell Cultures of *Pinctada fucata*. *PLoS One* **2014**, *9*, No. e113150.

(61) Yong Lee, S.; Kim, H.; Jang, H.; Hwang, M.-J.; Bong Lee, K.; Choi, J.-W.; Jung, K.-W. Fabrication of Manganese Ferrite (MnFe_2O_4) Microsphere-Coated Magnetic Biochar Composite for Antimonate Sequestration: Characterization, Adsorption Behavior, and Mechanistic Understanding. *Appl. Surf. Sci.* **2022**, *578*, 152005.

(62) Shaw, S. K.; Kailashiya, J.; Gupta, S. K.; Prajapat, C. L.; Meena, S. S.; Dash, D.; Maiti, P.; Prasad, N. K. MnFe_2O_4 Nano-Flower: A Prospective Material for Bimodal Hyperthermia. *J. Alloys Compd.* **2022**, *899*, 163192.

(63) Lucky, S. S.; Soo, K. C.; Zhang, Y. Nanoparticles in Photodynamic Therapy. *Chem. Rev.* **2015**, *115*, 1990–2042.

(64) Tkachenko, A. G.; Xie, H.; Liu, Y.; Coleman, D.; Ryan, J.; Glomm, W. R.; Shipton, M. K.; Franzen, S.; Feldheim, D. L. Cellular Trajectories of Peptide-Modified Gold Particle Complexes: Comparison of Nuclear Localization Signals and Peptide Transduction Domains. *Bioconjugate Chem.* **2004**, *15*, 482–490.

(65) Song, H.; Nor, Y. A.; Yu, M.; Yang, Y.; Zhang, J.; Zhang, H.; Xu, C.; Mitter, N.; Yu, C. Silica Nanopollens Enhance Adhesion for Long-Term Bacterial Inhibition. *J. Am. Chem. Soc.* **2016**, *138*, 6455–6462.

(66) Sougrat, R.; Bartesaghi, A.; Lifson, J. D.; Bennett, A. E.; Bess, J. W.; Zabransky, D. J.; Subramaniam, S. Electron Tomography of the

Contact between T Cells and SIV/HIV-1: Implications for Viral Entry. *PLoS Pathog.* **2007**, *3*, No. e63.

(67) Jain, S.; Coulter, J. A.; Butterworth, K. T.; Hounsell, A. R.; McMahon, S. J.; Hyland, W. B.; Muir, M. F.; Dickson, G. R.; Prise, K. M.; Currell, F. J.; Hirst, D. G.; O'Sullivan, J. M. Gold Nanoparticle Cellular Uptake, Toxicity and Radiosensitisation in Hypoxic Conditions. *Radiother. Oncol.* **2014**, *110*, 342–347.

(68) Griffiths, L.; Dachs, G. U.; Bicknell, R.; Harris, A. L.; Stratford, I. J. The Influence of Oxygen Tension and pH on the Expression of Platelet-derived Endothelial Cell Growth Factor/Thymidine Phosphorylase in Human Breast Tumor Cells Grown *In Vitro* and *In Vivo*. *Cancer Res.* **1997**, *57*, 570–572.

(69) Zhou, Y.; Fan, S.; Feng, L.; Huang, X.; Chen, X. Manipulating Intratumoral Fenton Chemistry for Enhanced Chemodynamic and Chemodynamic-Synergized Multimodal Therapy. *Adv. Mater.* **2021**, *33*, 2104223.

(70) Gottesman, M. M.; Fojo, T.; Bates, S. E. Multidrug Resistance in Cancer: Role of ATP-Dependent Transporters. *Nat. Rev. Cancer* **2002**, *2*, 48–58.

(71) AbuHammad, S.; Zihlif, M. Gene Expression Alterations in Doxorubicin Resistant MCF7 Breast Cancer Cell Line. *Genomics* **2013**, *101*, 213–220.

(72) Tsou, S. H.; Chen, T. M.; Hsiao, H. T.; Chen, Y. H. A Critical Dose of Doxorubicin is Required to Alter the Gene Expression Profiles in MCF-7 Cells Acquiring Multidrug Resistance. *PLoS One* **2015**, *10*, No. e0116747.

(73) Feng, Q.; Zhang, Y.; Shan, X.; Yuan, Y.; Zhang, H.; Hou, L.; Zhang, Z. Tumor-Targeted and Multi-Stimuli Responsive Drug Delivery System for Near-Infrared Light Induced Chemo-Phototherapy and Photoacoustic Tomography. *Acta Biomater.* **2016**, *38*, 129–142.

(74) Ou, W.; Nam, K. S.; Park, D. H.; Hwang, J.; Ku, S. K.; Yong, C. S.; Kim, J. O.; Byeon, J. H. Artificial Nanoscale Erythrocytes from Clinically Relevant Compounds for Enhancing Cancer Immunotherapy. *Nano-Micro Lett.* **2020**, *12*, 90.

(75) Dai, Y.; Yang, Z.; Cheng, S.; Wang, Z.; Zhang, R.; Zhu, G.; Wang, Z.; Yung, B. C.; Tian, R.; Jacobson, O.; Xu, C.; Ni, Q.; Song, J.; Sun, X.; Niu, G.; Chen, X. Toxic Reactive Oxygen Species Enhanced Synergistic Combination Therapy by Self-Assembled Metal-Phenolic Network Nanoparticles. *Adv. Mater.* **2018**, *30*, 1704877.

(76) Jin, R.; Liu, Z.; Bai, Y.; Zhou, Y.; Gooding, J. J.; Chen, X. Core-Satellite Mesoporous Silica-Gold Nanotheranostics for Biological Stimuli Triggered Multimodal Cancer Therapy. *Adv. Funct. Mater.* **2018**, *28*, 1801961.

(77) Ranji-Burachloo, H.; Gurr, P. A.; Dunstan, D. E.; Qiao, G. G. Cancer Treatment through Nanoparticle-Facilitated Fenton Reaction. *ACS Nano* **2018**, *12*, 11819–11837.

(78) Barua, S.; Yoo, J.-W.; Kolhar, P.; Wakankar, A.; Gokarn, Y. R.; Mitragori, S. Particle Shape Enhances Specificity of Antibody-Displaying Nanoparticles. *Proc. Natl. Acad. Sci. U.S.A.* **2013**, *110*, 3270–3275.

(79) Stieberova, B.; Zilka, M.; Ticha, M.; Freiberg, F.; Caramazana-González, P.; McKechnie, J.; Lester, E. Sustainability Assessment of Continuous-Flow Hydrothermal Synthesis of Nanomaterials in the Context of Other Production Technologies. *J. Clean. Prod.* **2019**, *241*, 118325.

(80) Kim, J.; Cho, H. R.; Jeon, H.; Kim, D.; Song, C.; Lee, N.; Choi, S. H.; Hyeon, T. Continuous O_2 -Evolving MnFe_2O_4 Nanoparticle-Anchored Mesoporous Silica Nanoparticles for Efficient Photodynamic Therapy in Hypoxic Cancer. *J. Am. Chem. Soc.* **2017**, *139*, 10992–10995.

(81) Gupta, B.; Ramasamy, T.; Poudel, B. K.; Pathak, S.; Regmi, S.; Choi, J. Y.; Son, Y.; Thapa, R. K.; Jeong, J.-H.; Kim, J. R.; Choi, H.-G.; Yong, C. S.; Kim, J. O. Development of Bioactive PEGylated Nanostructured Platforms for Sequential Delivery of Doxorubicin and Imatinib to Overcome Drug Resistance in Metastatic Tumors. *ACS Appl. Mater. Interfaces* **2017**, *9*, 9280–9290.

(82) Nguyen, H. T.; Phung, C. D.; Tran, T. H.; Pham, T. T.; Pham, L. M.; Nguyen, T. T.; Jeong, J.-H.; Choi, H.-G.; Ku, S. K.; Yong, C. S.;

Kim, J. O. Manipulating Immune System using Nanoparticles for an Effective Cancer Treatment: Combination of Targeted Therapy and Checkpoint Blockage miRNA. *J. Controlled Release* **2021**, 329, 524–537.

(83) Lan, G.; Ni, K.; Xu, Z.; Veroneau, S. S.; Song, Y.; Lin, W. Nanoscale Metal-Organic Framework Overcomes Hypoxia for Photodynamic Therapy Primed Cancer Immunotherapy. *J. Am. Chem. Soc.* **2018**, 140, 5670–5673.

(84) Liu, C.; Wang, D.; Zhang, S.; Cheng, Y.; Yang, F.; Xing, Y.; Xu, T.; Dong, H.; Zhang, X. Biodegradable Biomimic Copper/Manganese Silicate Nanospheres for Chemodynamic/Photodynamic Synergistic Therapy with Simultaneous Glutathione Depletion and Hypoxia Relief. *ACS Nano* **2019**, 13, 4267–4277.

(85) Ou, W.; Jiang, L.; Thapa, R. K.; Soe, Z. C.; Poudel, K.; Chang, J.-H.; Ku, S. K.; Choi, H.-G.; Yong, C. S.; Kim, J. O. Combination of NIR Therapy and Regulatory T Cell Modulation using Layer-by-Layer Hybrid Nanoparticles for Effective Cancer Photoimmunotherapy. *Theranostics* **2018**, 8, 4574–4590.

(86) Ou, W.; Jiang, L.; Gu, Y.; Soe, Z. C.; Kim, B. K.; Gautam, M.; Poudel, K.; Pham, L. M.; Phung, C. D.; Chang, J.-H.; Kim, J. R.; Ku, S. K.; Yong, C. S.; Kim, J. O. Regulatory T Cells Tailored with pH-Responsive Liposomes Shape an Immuno-Antitumor Milieu against Tumors. *ACS Appl. Mater. Interfaces* **2019**, 11, 36333–36346.